JGR Space Physics

RESEARCH ARTICLE
10.1029/2020JA028872

Multispacecraft Current Density Estimates in the Low- and Mid-Latitude F-Region Ionosphere Using the Swarm Constellation

M. Fillion[1], G. Hulot[1], P. Alken[2,3], A. Chulliat[2,3], and P. Vigneron[1]

[1]Institut de Physique du Globe de Paris, CNRS, Université de Paris, Paris, France, [2]Cooperative Institute for Research in Environmental Sciences, University of Colorado, Boulder, CO, USA, [3]NOAA National Centers for Environmental Information, Boulder, CO, USA

Key Points:

- A new application of a multispacecraft method to derive the three components of the current density in the F-region ionosphere is presented
- An assessment of the effect of biases and errors on the current density estimates is provided
- Application of the method on February 15, 2014 reveals both expected and new characteristics of F-region currents

Correspondence to:
M. Fillion,
fillion@ipgp.fr

Citation:
Fillion, M., Hulot, G., Alken, P., Chulliat, A., & Vigneron, P. (2021). Multispacecraft current density estimates in the low- and mid-latitude F-region ionosphere using the Swarm constellation. *Journal of Geophysical Research: Space Physics*, *126*, e2020JA028872. https://doi.org/10.1029/2020JA028872

Received 30 OCT 2020
Accepted 1 JUN 2021

Abstract We present a new application of a multispacecraft method which provides estimates of the full electric current density vector in the ionospheric low- and mid-latitude F region. The method uses the three satellites of the Swarm constellation in configurations when they were close to each other. The current density is calculated inside triangular prisms defined by the satellite positions. The technique is inspired by similar approaches such as the *curlometer*. Here, we propose an alternative mathematical treatment, which involves the use of the well-known curl-B technique and a least squares minimization. The proposed formalism provides a rigorous way to propagate the errors through the problem and special care is taken to validate the algorithm and assess the relevance of the derived currents. Such techniques are powerful tools to study the F-region ionosphere currents as they naturally exclude all the other contributions outside the considered volumes. The F region is known to host currents with a complex spatiotemporal variability. Besides the intrinsic interest of this system itself, understanding the dynamics of these currents is also critical for global geomagnetic field modeling as they are an important source of error in the models. In this paper, we present the full algorithm and test the method on both synthetic and real Swarm satellite data on February 15, 2014. Several sources of error are investigated. Additionally, the results reveal expected characteristics of F-region interhemispheric field-aligned currents. Some new characteristics of F-region currents, potentially associated with dynamo and pressure currents, are also observed.

1. Introduction

The Earth's ionosphere is the ionized layer of the Earth's atmosphere. It ranges approximately from 80 to 1,000 km. In this region, large-scale currents arise as a result of interactions between the plasma, the ambient Earth's magnetic field, electric fields, plasma pressure gradient, and external forces that act on the system, such as neutral wind friction and gravity. The ionosphere is classically divided into three regions: the D, the E, and the F region (Kelley, 2009). The latter, which ranges from 150 to 1,000 km, is the region of interest in this study.

Thermospheric winds in the low- and mid-latitude F-region generate currents through a mechanism known as the "F-region dynamo" (Rishbeth, 1971a, 1971b, 1981). These winds blow the plasma across the Earth's magnetic field lines, which produce an electromotive force resulting in electrical currents and polarization electric fields (Richmond, 1995b). Features of the F-layer dynamo were reviewed by Rishbeth (1997) and more recently by Maute and Richmond (2017b) using a three-dimensional physics-based model.

Additional currents driven by gravity and plasma pressure gradients also flow in the F region. These currents were reviewed by Alken et al. (2017). Gravity currents arise because the $\vec{g} \times \vec{B}$ drift (where $\vec{g}$ and $\vec{B}$ are respectively, the acceleration of gravity and the Earth magnetic field) of a charged particle depends on the sign of the electric charge, leading ions and electrons to drift in opposite directions. Their intensity depends on the plasma density. Such currents were identified in satellite magnetic field measurements near the F-region electron density peak using CHAMP data (Maus & Lühr, 2006) and a combination of CHAMP and SWARM data (Alken, 2016). Plasma pressure currents are different and depend on the plasma density gradients. Such gradients also generate a differential drift of ions and electrons, now in the $\vec{\nabla} n \times \vec{B}$ direction (where n stands for the plasma density) leading to a net current. The pressure currents are diamagnetic, that

is, they reduce the ambient geomagnetic field. Lühr et al. (2003) have detected magnetic field weakening in CHAMP measurements attributed to such currents.

Interhemispheric field-aligned currents are also detected in the F-region at LEO satellite altitudes (Lühr et al., 2015). These currents balance the electrostatic potential difference in the E-region between the northern and southern Sq current systems that arises from the asymmetric dynamo action between the two hemispheres (Fukushima, 1979; Takeda, 1982). Numerical simulations pointed out that the direction of these currents depends on both season and local time (Takeda, 1982; van Sabben, 1970). Since then, this current system has been the subject of many data-based studies (Abidin et al., 2019; Bolaji et al., 2012; Fathy et al., 2019; Lühr et al., 2015, 2019; Olsen, 1997; Park et al., 2011; Yamashita & Iyemori, 2002), which have revealed a rather complex climatology.

In this study, we present a new approach to estimate the full current density vector using the three Swarm satellites. The method is inspired by similar multispacecraft approaches. Among them, the *curlometer* technique (Dunlop, Southwood, et al., 1988) has been widely used. It consists of a direct calculation of the local average current density using a discretized form of the Ampere integral law. It was applied to both the Cluster and Swarm satellite constellations to investigate magnetospheric and high-latitude ionospheric field-aligned currents (Dunlop et al., 2002; Dunlop et al., 2015a; Dunlop et al., 2015b; Shen et al., 2014). Some other approaches are referred to as *local least square* techniques (De Keyser et al., 2007; Vogt et al., 2013, 2020). They rely on least square estimations of the magnetic field spatial derivatives (Harvey, 1998; Vogt et al., 2008) which can subsequently be used to infer the local current density using the Ampere differential law. The mathematical formalism of our new approach, however, differs from both that of the curlometer and local least square techniques. First, in contrast with the curlometer, it relies on a least square estimation technique. Second, as opposed to local least square techniques, it provides least square estimations of the current density itself rather than least square estimations of the magnetic field spatial derivatives.

In this paper, we investigate low- and mid-latitude F-region currents during February 15, 2014 using our new approach and magnetometer data from the Swarm mission (Friis-Christensen et al., 2006). In Section 2, we first describe the data selection and preprocessing needed to implement our algorithm, next presented in Section 3. In Section 4, the methodology to characterize the errors affecting the Swarm data is presented. The method is next tested using synthetic Swarm satellite data in Section 5, and applied to real Swarm satellite data in Section 6 where the results are discussed. Section 7 concludes this paper.

2. Data Pre-Processing and Selection

The Swarm constellation was launched on November 22, 2013 and consists of three identical satellites named Alpha, Bravo, and Charlie (Friis-Christensen et al., 2006). The three satellites reached their final orbit in May 2014; Alpha and Charlie were lowered at an average altitude of 460 km and now fly on closeby orbits whereas Bravo was raised to an average altitude of 530 km. This study, however, focuses on February 15, 2014 when the configuration of the constellation was different. On that day, Swarm Alpha had an average altitude of 480 km whereas Swarm Bravo and Charlie orbited a little higher, at roughly 500 km. All three satellites were close to each other on a near-polar orbit. They covered the morning sector (roughly 06:00–08:00 LT) during the ascending phase and the evening sector (roughly 18:00–20:00 LT) during the descending phase.

All three satellites carry a vector field magnetometer (VFM) and an absolute scalar magnetometer (ASM), which measure the vector and the intensity of the geomagnetic field, respectively. The Swarm data processing chain provides the Level 1-b magnetic field scalar and vector 1-Hz measurements used in this study. Specifically, we make use of the MAG_LR level 1-b product version 0505 for the three Swarm satellites on February 15, 2014. To best isolate the magnetic field generated by F-region currents, we first calculate the vector residuals by taking the difference between the vector magnetic field measurements and the Swarm-derived potential field representations of the core, lithospheric, ionospheric E-region and magnetospheric fields from the Comprehensive Model (Sabaka et al., 2018) version 0501. We then remove outliers defined as data having a difference greater than 10 nT with both the preceding and following data. Because the data time series will be further decimated every 5 s in Section 3.1, the resulting data set is low-pass filtered using a

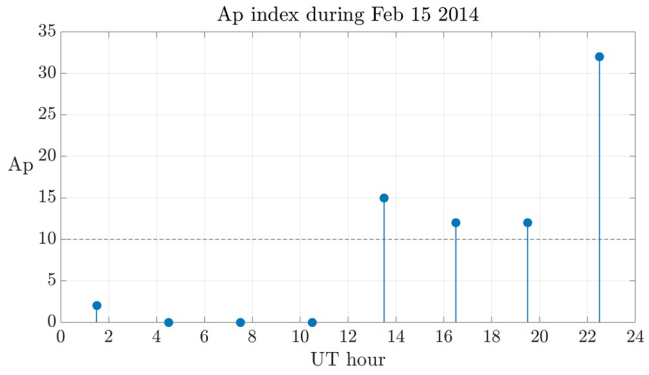

Figure 1. 3-h Ap index during February 15, 2014. The black-dashed line marks the selection criterion Ap ≤ 10.

second order Butterworth filter with a cutoff period of 20 s at 3 dB to avoid aliasing. Finally, data are selected for geomagnetically quiet times and low and mid quasi-dipole latitudes (Richmond, 1995a) with the requirements that the 3-h Ap index is less than 10 and the quasi-dipole latitude is between ±50°. In particular, the first selection criteria imply that only data between 0 and 13 UTC are retained (see Figure 1). In the following, the processed data set will be termed "magnetic dataset" and a data from this data set "magnetic data."

3. Methodology

3.1. Formation of Prisms

Estimating the average current density requires that the three Swarm satellites fly in close formation. The method presented here calculates the average current density that flows through triangular prisms whose vertices are defined with successive positions of the three Swarm satellites (Figure 2). To build such prisms, the entire magnetic data set is explored to find times and locations where Alpha, Bravo, and Charlie are close to each other. In particular, we require that (1) each pair of satellites is separated by less than 1° in quasi-dipole latitude and 3° in quasi-dipole longitude, (2) one satellite flies at least 18 km above or under the two others, and (3) the time difference between the satellite measurements must be less than 180 s. These criteria are summarized in Table 1. In practice, the satellite Bravo is taken to be the reference satellite and at each time all the criteria are sequentially tested for both satellites Alpha and Charlie. For a given time, if more than one configuration of satellites satisfy these criteria, the selected configuration is the one for which Alpha and Charlie satellites are the closest to Bravo in terms of quasi-dipole latitude. With all the selected configurations, triangular prisms are formed using successive configurations of satellites such that successive data from the same satellite within one prism are separated by 5 s (see Figure 2). This operation implicitly implies the decimation of the data time series of the Swarm satellites every 5 s. During the day of interest, February 15, 2014, and during geomagnetically quiet times, we were able to form 4,176 prisms.

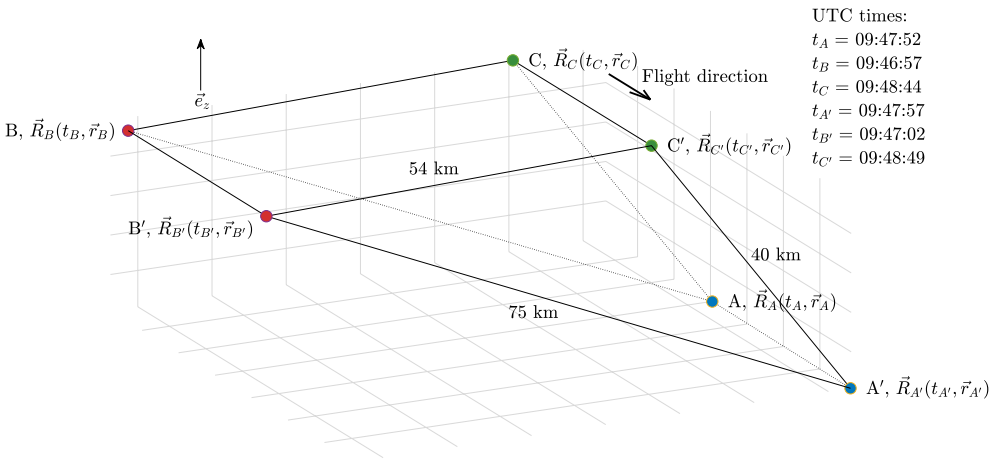

Figure 2. An example of a triangular prism represented at scale and built using two successive positions of the three satellites Alpha, Bravo, and Charlie separated by 5 s on February 15, 2014. Here, the prime superscripts refer to the final positions. At each vertex, there is a magnetic data denoted $\vec{R}_q$, where q can be either A, B, or C, respectively corresponding to satellites Alpha, Bravo, and Charlie. The magnetic data associated with the satellite q depends on the time t_q and its position vector $\vec{r}_q$. In general, $t_A \neq t_B \neq t_C$ and $t_{A'} \neq t_{B'} \neq t_{C'}$. The $\vec{e}_z$ vector shows the local vertical and the lengths of the three sides of the triangular base are given in km.

Table 1
Criteria to Define a Valid Configuration of Three Satellites

All pairs of satellites must satisfy	Two pairs of satellites must satisfy
$\Delta t \leq 180s$ $\Delta\theta_q \leq 1°$ $\Delta\phi_q \leq 3°$	$\Delta r \geq 18$ km

Note. Here, t is the time, r the radius, θ_q, ϕ_q the quasi-dipole latitude and longitude and Δt, $\Delta\theta_q$, $\Delta\phi_q$ and Δr stand for the difference of these quantities between two satellites.

3.2. Integral Version of the Curl-B Technique Applied to Prisms

The method presented here makes use of the integral version of the Curl-B technique first introduced by Ritter and Lühr (2006). This technique is based on an Ampere contour integral:

$$j = \frac{1}{\mu_0 S} \oint \vec{B} \cdot \vec{dl} \tag{1}$$

where μ_0 is the vacuum permeability, S is the area defined by the contour, and j is the current density that flows through this surface. The technique provides the average current density j through a polygonal surface with the requirement that a vector magnetic field measurement is available at each vertex. On each side of the surface, the infinitesimal element $\vec{B} \cdot \vec{dl}$ is taken to be constant and given by the average of the projections of the magnetic data at the edges on the $\vec{dl}$ vector, which defines the direction of integration. Figure 3 illustrates how this technique works by taking a triangle as an example. In this example, the infinitesimal element is taken to be the average of the blue (resp. green and red) projections on the segment AB (resp. BC and AC). The average current density that flows through the triangle in this figure may be expressed as:

$$\begin{aligned} j \;= & \frac{1}{2\mu_0 S}\Big[(\vec{B}_A \cdot \vec{u}_{AB} + \vec{B}_B \cdot \vec{u}_{AB})l_{AB} + (\vec{B}_B \cdot \vec{u}_{BC} + \vec{B}_C \cdot \vec{u}_{BC})l_{BC} \\ & + \left(\vec{B}_C \cdot \vec{u}_{CA} + \vec{B}_A \cdot \vec{u}_{CA}\right)l_{CA}\Big] \end{aligned} \tag{2}$$

where $\vec{u}_{QP}$, Q, and P being either A, B, or C, is a unit vector oriented from the point Q toward P, l_{QP} is the length of the segment QP and S is the area of the triangle.

The Curl-B technique has been used to study the average local time variation of F-region zonal currents (Lühr et al., 2016) and F-region radial and interhemispheric currents (Fathy et al., 2019; Lühr et al., 2015, 2019). In this study, we take the technique one step further and use it to calculate the average current density that flows through each of the five surfaces of the prism, that is, two triangles and three four-sided polygons. Using Equation 1 for each surface and writing all five equations in matrix form gives:

$$\vec{j}_p = \mathbf{G_j}\vec{R} \tag{3}$$

where $\vec{j}_p$ is a (5×1) column vector that contains the average current density through the five prism's surfaces, the subscript p standing for *prism*, $\vec{R}$ is a (18×1) vector that contains the three components of the six magnetic data at the vertexes of the prism, and $\mathbf{G_j}$ maps the $\vec{R}$ vector to the $\vec{j}_p$ vector (see Appendices A1 and A2 for details on $\vec{j}_p$, $\vec{R}$ and the $\mathbf{G_j}$ operator). Each prism is then associated with a vector $\vec{j}_p$. Note here that the application of the curl-B technique to the prisms requires making two assumptions. First, the magnetic field varies linearly inside the prism. Second, the magnetic field is stationary over 180 s corresponding to the maximum time lag between two magnetic data. In this paper, we will refer to magnetic fields that, to some extent, do not satisfy these two conditions as *nonlinear* and *nonstationary* magnetic fields.

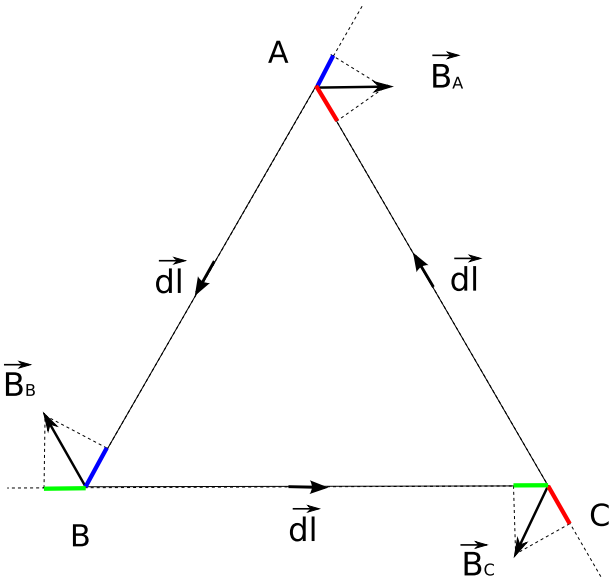

Figure 3. Illustration of the Curl-B calculation of the average current density through a triangle. The infinitesimal element $\vec{B} \cdot \vec{dl}$ of the contour integral is taken to be the average of the blue projections on the segment AB, the reds on the segment AC and the greens on the segment BC.

3.3. Error Propagation on the $\vec{j}_p$ Vector

Level-1b Swarm magnetic measurements are affected by instrumental noise and satellite perturbations, the former potentially introducing slowly varying biases. Of particular concern is the Sun-driven disturbance field. This field originates from currents driven on the satellite by temperature gradients in the vicinity of the magnetometers. It was

identified using the scalar residuals, defined as the difference between the modulus of the VFM vector measurement and the ASM scalar measurement. These residuals have been found to be systematically dependent on the Sun incidence angle (Lesur et al., 2015; Tøffner-Clausen et al., 2016). This effect can be partially corrected empirically by using a least-square minimization of the scalar residuals (Tøffner-Clausen et al., 2016). This correction, to which we will refer as the *dBSun* correction, is routinely applied to the Level-1b Swarm data version 0505 used in this study.

Slowly varying biases and instrumental noise propagate to the data vector $\vec{j}_p$ through Equation 3. Following Ritter et al. (2013) and Lühr et al. (2016), we consider that each element of the $\vec{R}$ vector is affected by a bias assumed to be constant over a short period of time, typically the 5 s between the successive positions of the Swarm satellites, combined with a statistically independent random noise. One component of two successive measurements from the same Swarm satellite shares the same bias. The bias and the random noise add up to the total error on the magnetic data. The position errors are assumed to be negligible. Additionally, we do not consider errors associated with nonlinear and nonstationary magnetic fields. These errors will be further discussed in Section 5.

In this study, both the bias and the random noise are described as the result of random Gaussian processes. Considering a bias as the realization of a random process might seem counterintuitive, however, it can be shown that if two measurements share a common bias, this bias can be regarded as a fully correlated random error (Barlow, 1989). This implies that the covariance between two data with a common bias is given by the square of the bias standard deviation. With these considerations in mind, one can build a data covariance matrix $\mathbf{C_R}$ associated with the $\vec{R}$ vector of Equation 3:

$$C_{R,lk} = \begin{cases} \sigma_{bias}^2 + \sigma_{error}^2, & \text{if } l = k \\ \sigma_{bias}^2, & R_l \text{ and } R_k \text{ sharing a common bias} \\ 0, & \text{otherwise} \end{cases} \tag{4}$$

where $C_{R,lk}$ is the element at the lth row and the kth column of the $\mathbf{C_R}$ matrix, l and k ranging from 1 to 18, R_l and R_k are the lth and kth elements of the $\vec{R}$ vector and σ_{bias} and σ_{error} are respectively the standard deviations associated with the bias and the random error. The description of the procedure to set numerical values for σ_{bias} and σ_{error} is postponed to Section 4. Each prism has a corresponding $\mathbf{C_R}$ matrix. The $\mathbf{C_R}$ covariance matrix propagates in Equation 3 through:

$$\mathbf{C_j} = \mathbf{G_j C_R G_j^t} \tag{5}$$

where $\mathbf{C_j}$ is the data covariance matrix associated with the vector $\vec{j}_p$.

3.4. Inverse Problem

The method aims at recovering the full current density vector flowing through the prisms defined in Section 3.1. The algorithm is based on the assumption that this current density is uniform. The parameter vector is the vector whose elements are the three components of the uniform current. Figure 4 illustrates the configuration. Through each prism flows a current density $\vec{J}$ and we can define one unit normal vector $\vec{n}$ on each of the five surfaces. The parameter vector is estimated by minimizing the square of the difference between the current fluxes through the five surfaces of the prism (i.e., the five component data vector $\vec{j}_p$, calculated with the curl-B technique, Section 3.2) and the corresponding predicted fluxes, calculated by projecting $\vec{J}$ on the five normal vectors $\vec{n}_i$. The forward problem can be written as:

$$\vec{j}_p = \mathbf{G}\vec{J} \tag{6}$$

where $\vec{j}_p$ is the (5×1) vector from Section 3.2, $\vec{J}$ is a (3×1) vector which stands for the three components of the uniform current and $\mathbf{G}$ is a linear map. Expressions for $\vec{j}_p$, $\vec{J}$ and $\mathbf{G}$ are given in Appendices A2 and A3. The inverse problem is solved in a least square sense with:

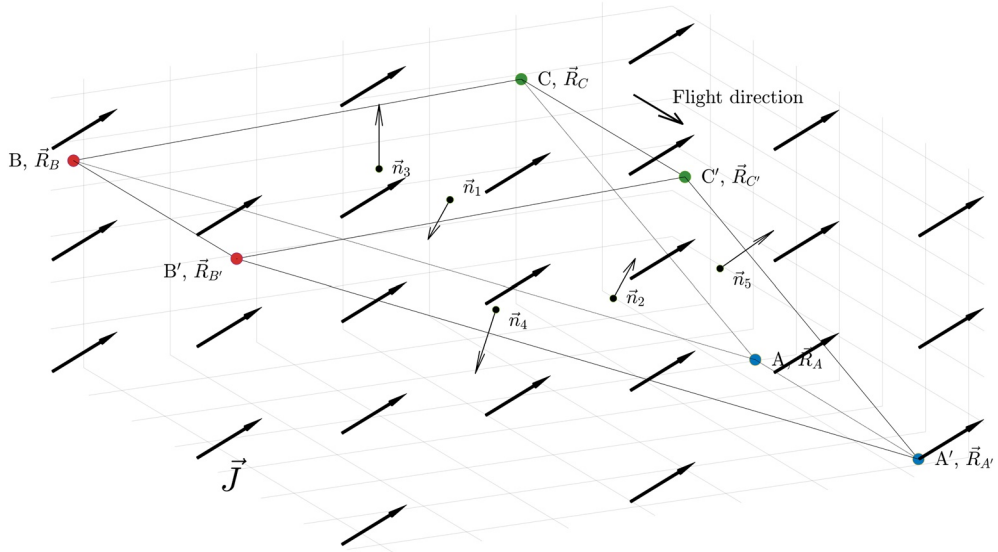

Figure 4. Illustration of the forward problem using the prism shown in Figure 2. A current of current density $\vec{J}$, illustrated by the black arrows, flows through the prism and is assumed to be uniform. One normal unit vector $\vec{n}_i$ is associated with the ith surface, i ranging from 1 to 5. The forward problem is defined such that the flux of the current through each surface i must equal the projection of the $\vec{J}$ vector on the corresponding normal vector $\vec{n}_i$ multiplied by the area of the ith surface.

$$\vec{J} = (\mathbf{G}^t\mathbf{C}_\mathbf{j}^{-1}\mathbf{G})^{-1}\mathbf{G}^t\mathbf{C}_\mathbf{j}^{-1}\vec{\jmath}_p \tag{7}$$

where $\mathbf{C_j}$ is the covariance matrix in the data space defined in Section 3.3. The a posteriori (3×3) covariance matrix $\mathbf{C_J}$ can be calculated with:

$$\mathbf{C_J} = (\mathbf{G}^t\mathbf{C}_\mathbf{j}^{-1}\mathbf{G})^{-1} \tag{8}$$

3.5. Inversion of the $\mathbf{C_j}$ Matrix

In the ionosphere, a tiny departure from charge neutrality generates instantaneously strong electric fields such that it maintains a null divergence of the current density. Applying the divergence theorem in the ionosphere then gives:

$$\iiint_V \vec{\nabla} \cdot \vec{\jmath}\, dV = \oiint_S \vec{\jmath} \cdot \vec{n}\, dS = 0 \tag{9}$$

This theorem can be applied on the prism presented in Figure 4 which leads to:

$$S_1 j_{p1} + S_2 j_{p2} + S_3 j_{p3} + S_4 j_{p4} + S_5 j_{p5} = 0 \tag{10}$$

where $S_{1..5}$ and $j_{p1..5}$ are respectively the areas of the prism faces of normal vectors $\vec{n}_{1..5}$ and the current density through these surfaces. Equation 10 implies that one element of the data vector $\vec{\jmath}_p$ can be expressed as a linear combination of the others. Interestingly, Equation 10 is true regardless of the bias and errors affecting the magnetic data in the vector $\vec{R}$ which were used to calculate the vector $\vec{\jmath}_p$ in Equation 3. This can be verified by expressing each element $j_{p1..5}$ as a function of the magnetic data, such as was done in Equation 2, and then injecting these expressions in Equation 10. In fact, we can go even further and state that if the magnetic data were dominated by errors Equation 10 would still be strictly true. This is because the error on one element among $j_{p1..5}$ can also be expressed as a linear combination of the errors on the others. It implies that one column of the $\mathbf{C_j}$ matrix can be expressed as a linear combination of the others which in turn means that this matrix is singular.

The estimation of the uniform current density with our method nevertheless requires calculating the inverse of the $\mathbf{C_j}$ matrix (Equations 7 and 8). This can be done in terms of a minimum norm solution using a singular value decomposition (SVD) such as described in Press et al. (1989b). The SVD of the $\mathbf{C_j}$ matrix gives:

$$\mathbf{C_j} = \mathbf{U_j D_j V_j^t} \tag{11}$$

where $\mathbf{C_j}$, $\mathbf{U_j}$, and $\mathbf{V_j}$ are square (5×5) matrices and $\mathbf{D_j}$ is a diagonal matrix which contains the singular values of the $\mathbf{C_j}$ matrix. Its inverse is calculated with:

$$\mathbf{C_j^{-1}} = \mathbf{V_j D_j^{-1} U_j^t} \tag{12}$$

where the inverse of $\mathbf{D_j}$ is obtained by taking the inverse of the singular values and placing them in the diagonal elements. Because $\mathbf{C_j}$ is singular, a problem arises in the calculation of $\mathbf{D_j^{-1}}$ because of zero singular values. A minimum-norm solution can nevertheless be found by setting the inverse of zero singular values to zero. Note that this is equivalent to discard one linear combination of the elements of the data vector $\vec{J}_p$ corresponding to Equation 10, which is a redundant information. Equation 12 then becomes:

$$\mathbf{C_j^{-1}} = \mathbf{V_j D_{mod,j}^{-1} U_j^t} \tag{13}$$

where $\mathbf{D_{mod,j}}$ is the $\mathbf{D_j}$ matrix for which the inverse of the zero singular value has been set to zero.

Using now all the quantities defined in Sections 3.2, 3.3, 3.4 and 3.5, one can write for each prism the full equation linking the magnetic data vector $\vec{R}$ to the uniform current $\vec{J}$:

$$\vec{J} = (\mathbf{G^t V_j D_{mod,j}^{-1} U_j^t G})^{-1} \mathbf{G^t V_j D_{mod,j}^{-1} U_j^t G_j} \vec{R} \tag{14}$$

where setting the smallest diagonal element of $\mathbf{D_{mod,j}^{-1}}$ to zero accounts for the requirement that Equation 10 must be satisfied.

4. Numerical Values of the $\mathbf{C_R}$ Matrix Elements

4.1. Information Contained in the Scalar Residuals

To perform the calculation described in Section 3, one must find an appropriate method to set realistic values of the $\mathbf{C_R}$ matrix elements (Section 3.3), that is the standard deviations associated to the bias σ_{bias} and the random error σ_{error}. The scalar residuals (Section 3.3), usually denoted ΔF, can provide constraints in this regard. They contain mixed information on the biases and errors that affect the VFM and ASM instruments. More specifically, they contain two contributions. First, the projection of the bias perturbation vectors in the direction of the main field. Second, a contribution from a noise which results from the difference between the instrumental noise in the modulus of the VFM measurements and in the ASM measurements.

Figure 5 presents these residuals for all three Swarm satellites during February 15, 2014 at quiet times calculated with version 0505 Swarm data (Section 3.3). They display some slow-varying patterns which confirm the occurrence of remaining slow-varying biases in the Swarm data. These patterns also have a clear orbital periodicity whose periods are highlighted by the black dashed vertical bars in Figure 5. This periodicity reflects a dependence on the Sun incidence angle characteristic of likely residual dBSun perturbations. The scalar residuals also contain the expected random noise as can be observed in Figure 5.

We analyze independently these two contributions by temporally separating them, assuming that the random noise varies much more rapidly than the slow varying biases. The separation was achieved by low-pass filtering the scalar residuals for all three Swarm satellites with the same filter as the one used in Section 2. Figure 6 presents the separation procedure for Swarm satellite A during February 15, 2014 at quiet times. The top, middle and bottom panels respectively display the initial scalar residuals (same curve as the first panel of Figure 5), the filtered scalar residuals and the residual noise calculated by taking the difference between the initial scalar residuals and the filtered scalar residuals.

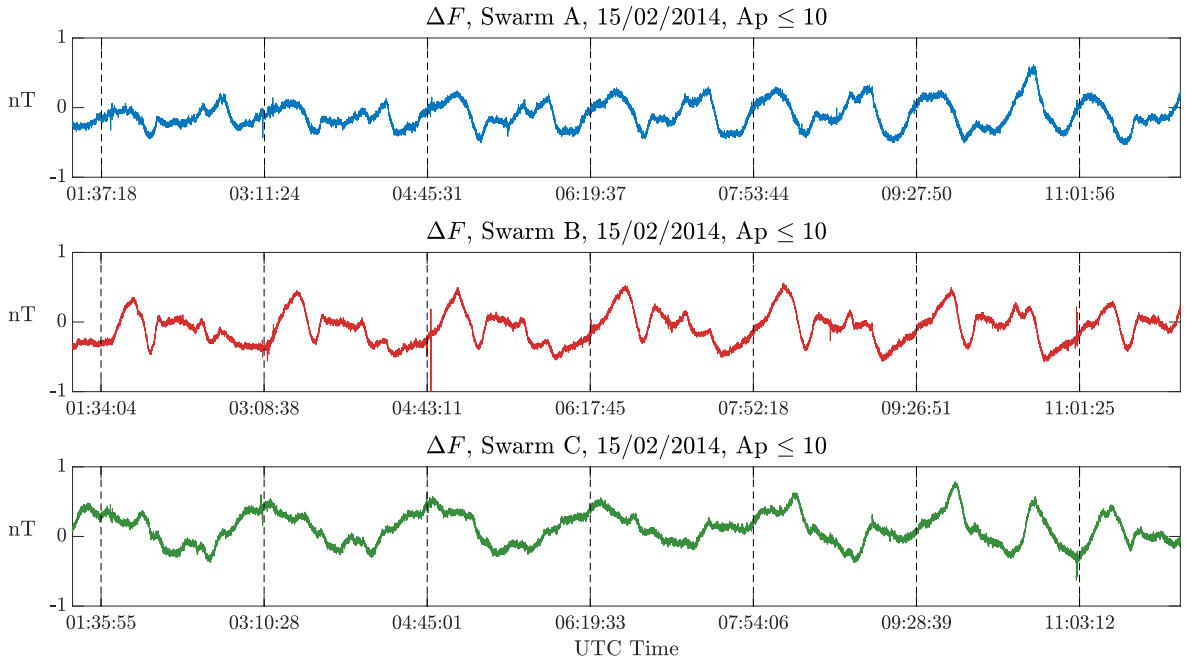

Figure 5. Scalar residuals ΔF on Swarm satellite A (top panel), B (middle panel), and C (bottom panel) calculated with version 0505 data during February 15, 2014 at quiet times. The black vertical dashed lines mark the times at which the satellites have completed a full orbit.

4.2. Choosing a Numerical Value for σ_{bias}

The filtered scalar residuals (second panel of Figure 6 for Swarm satellite A) are used to set a numerical value for the standard deviation σ_{bias}. This σ_{bias} characterizes the dispersion of the components of the bias vector, which is equivalent to characterizing the dispersion of the projection of the bias vector in a specific

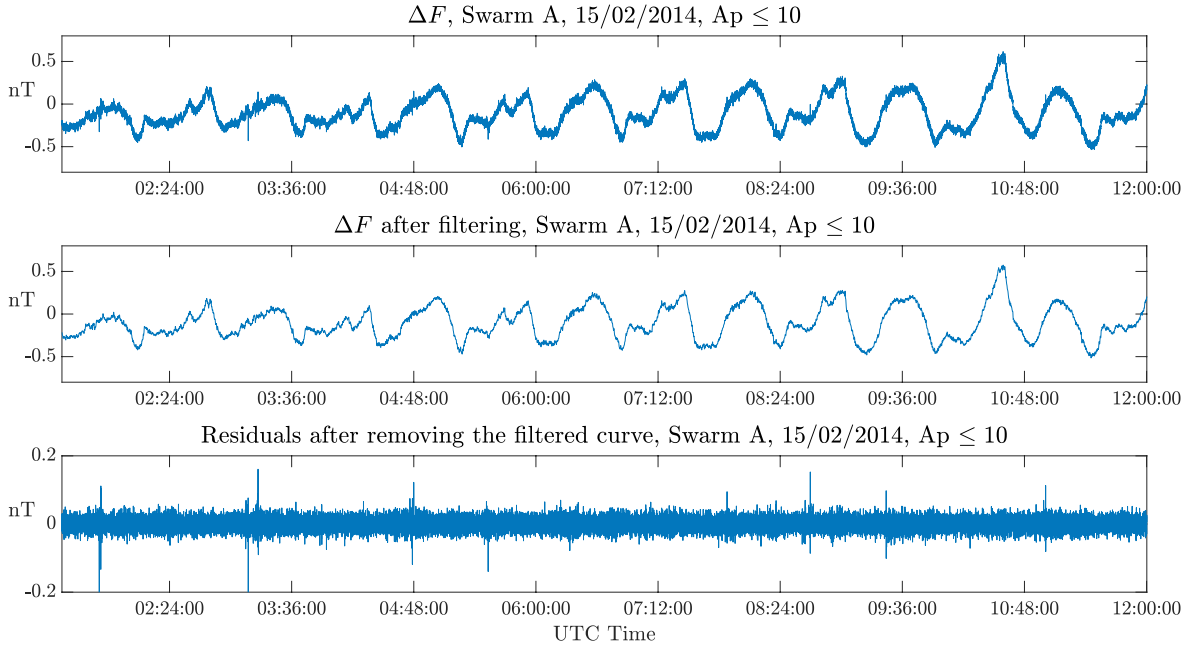

Figure 6. Scalar residuals ΔF (top panel, same as Figure 5), scalar residuals after filtering with a second order Butterworth filter with a cutoff period of 20 s at 3 dB (middle panel) and residual noise (bottom panel) calculated by taking the difference between the scalar residuals and the filtered scalar residuals for Swarm satellite A during February 15, 2014 at quiet times.

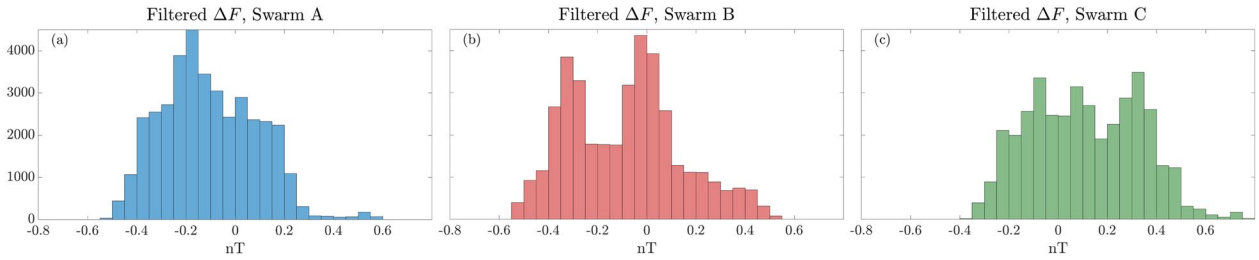

Figure 7. Histograms of the 1-Hz filtered scalar residuals during February 15, 2014 at quiet times for (a) Swarm satellite A, (b) Swarm satellite B, and (c) Swarm satellite C.

direction. Recalling that the filtered scalar residuals are an estimation of the projection of the bias vector in the direction of the main field, it turns out that they provide a straightforward means to estimate σ_{bias}.

Figure 7 shows histograms of the filtered scalar residuals for Swarm satellites A, B, and C during February 15, 2014 at quiet times. The non-Gaussian shapes of the distributions with the occurrence of one or multiple peaks are something to be expected. Indeed, in this study, we only look at a specific day during which the Swarm satellites explore the morning and evening sectors. Therefore, under these specific conditions, the biases might favor certain orientations and intensities. The distributions are not centered either and calculating directly their standard deviations would lead to underestimate σ_{bias}. The formalism of our method still requires the bias to be described as a Gaussian process and we must give a non-null probability to occur to every values in the histograms. To do so, we first compute the root mean square (RMS) of the scalar residuals ΔF for the three Swarm satellites, that is the quantity:

$$RMS_q = \sqrt{\frac{1}{N}\sum_{i=1}^{N}(\Delta F_{q,i})^2} \tag{15}$$

where RMS_q is the root mean square corresponding to Swarm satellite q, q being either A, B, or C standing respectively for Swarm satellites Alpha, Bravo, and Charlie, $\Delta F_{q,i}$ is the ith scalar residual of satellite q and N is the total number of scalar residuals. Using the scalar residuals presented in Figure 7, we respectively find $RMS_A \approx 0.21$, $RMS_B \approx 0.24$, and $RMS_C \approx 0.24$ nT. We then identify each value as an estimate of σ_{bias}. For each satellite, note that this is equivalent to symmetrize the histograms shown in Figure 7 and to approximate the resulting histograms with a Gaussian distribution. Because the three calculated RMS values are very close, we finally choose to set σ_{bias} to 0.25 nT such that it corresponds to an upper limit of these values.

4.3. Discussion on σ_{error}

The estimation of σ_{error} requires to consider two contributions. The first is the contribution of the instrumental noise. The second is the contribution of noises introduced by high frequency ionospheric signals, which are rejected by our inversion procedure because they violate the uniform current density assumption in the prisms (Section 3.4). It is therefore the combination of these two sources of noise that σ_{error} must reflect.

Table 2
Standard Deviation of the Noise in nT Extracted From the 1-Hz Scalar Residuals and of the Simulated Noise

	Swarm A	Swarm B	Swarm C
σ (nT)[a]	0.0163	0.0135	0.0167
σ_f (nT)[b]	0.0047	0.0039	0.0048

[a]σ stands for the standard deviation of the noise extracted from the 1-Hz scalar residuals during February 15, 2014 and quiet times. [b]σ_f stands for the standard deviation of the simulated noise generated with a Gaussian random process of mean 0 and SD given by the first row, and filtered using a second order Butterworth filter with a cutoff period of 20 s at 3 dB for each Swarm satellite.

We first characterize instrumental noise. Following the same line of argument as for σ_{bias} in Section 4.2, the noise extracted from the scalar residuals (third panel of Figure 6 for Swarm satellite A) provides an estimation of the instrumental noise on the components of the magnetic data. The first row of Table 2 shows the standard deviations of the noise extracted from the scalar residuals for the three Swarm satellites. We observe that these values, taking an upper limit, suggest an instrumental noise of the order of 0.02 nT.

An additional difficulty arises regarding the characterization of instrumental noise. This noise is indeed affected by the processing of the Swarm vector data in Section 2, which filters the data. The resulting magnetic data are used as inputs in the inverse problem. Therefore, rather than

the original instrumental noise on the Swarm vector data, σ_{error} must reflect the instrumental noise on the magnetic data. To estimate the resulting dispersion after the processing, we simulated a noise for each satellite by calculating 1 million realizations of a Gaussian random process with mean 0 and standard deviation given by the first row of Table 2. This simulated noise was subsequently filtered using the same filter as in Section 2, that is, a second order Butterworth filter with a cutoff period of 20 s at 3 dB, and the standard deviation of the resulting attenuated noise is given in the second row of Table 2. It is reduced to roughly 0.005 nT.

The second source of noise, which originates from high-frequency ionospheric signals, does not affect the scalar residuals, since both the VFM and ASM instruments simultaneously sense these signals. An alternative approach is needed to take this source of noise into account. In Sections 4.4 and 4.5, we present a method to set a value to σ_{error}. This method will also allow us to check that the value we attributed to σ_{bias} is relevant.

4.4. Chi-Square Goodness of Fit Test

The approach used to define a value for σ_{error} is to set this value according to the residuals of the inverse problems (Section 3.4). This can be done using a chi-square goodness of fit test such as described by Press et al. (1989a). Within the framework of this study, the chi-square is the quantity:

$$\chi^2 = \vec{\epsilon}^{\,t}\mathbf{C}_{\mathbf{j}}^{-1}\vec{\epsilon} \tag{16}$$

where $\vec{\epsilon}$ is the (5×1) residual column vector whose elements are given by:

$$\epsilon_i = j_{p,i} - \vec{J} \cdot \vec{n}_i \tag{17}$$

where i ranges from 1 to 5, ϵ_i and $j_{p,i}$ are respectively the ith components of the residual vector and the $\vec{j}_p$ vector, $\vec{n}_i$ is the vector normal to the surface i and $\vec{J}$ is the uniform current.

For a given inverse problem where the data are statistically independent, the chi-square is known to follow a chi-square distribution. This statement still holds for statistically correlated data since the chi-square can always be expressed as the sum of squared independent variables (Johnson & Wichern, 2002). Thus, the quantity in Equation 16 is also expected to follow a chi-square distribution. The number of degrees of freedom is given by the number of independent data minus the number of parameters of the problem. The inverse problem we deal with has three parameters, the three components of the uniform current $\vec{J}$, and five data, the five elements of the $\vec{j}_p$ vector. In Section 3.5, we showed that, because the divergence of the current density in the ionosphere is required to be null, each element of the $\vec{j}_p$ vector can be expressed as a linear combination of the others. This in turn implies that only four among the five elements of the $\vec{j}_p$ vector are statistically independent and that the chi-square has only 1 degree of freedom.

Traditionally, the chi-square goodness of fit is performed by calculating first the χ^2 and then the probability that it exceeds the calculated value given the number of degrees of freedom of the problem. In the present problem, we have at our disposal many realizations, one for each prism, of very similar inverse problems. Therefore the distribution obtained with the chi-squares calculated for all inverse problems must be close to a chi-square distribution with 1 degree of freedom provided that (a) the model represents well the data and (b) the standard deviations σ_{bias} and σ_{error} are well chosen. In Section 4.5, the second requirement will be worked backward and we explore which values of σ_{bias} and σ_{error} are optimal such that the obtained chi-square distribution is as close as possible to a degree one chi-square distribution. This method provides both a value for σ_{error} and a way to check that the value of σ_{bias} proposed in Section 4.2 is relevant.

4.5. Optimal Values of σ_{bias} and σ_{error}

To find optimal values of σ_{bias} and σ_{error}, we explore numerically the two-dimensional space in which one dimension corresponds to values of σ_{bias} and the second to values of σ_{error}. This space is sampled every 0.1 nT between 0 and 4 nT in the direction of σ_{bias} and every 0.01 nT between 0 and 0.3 nT in the direction of σ_{error}. We then test iteratively all possible combinations of values (σ_{bias}, σ_{error}) in the sampled space by, at each iteration,

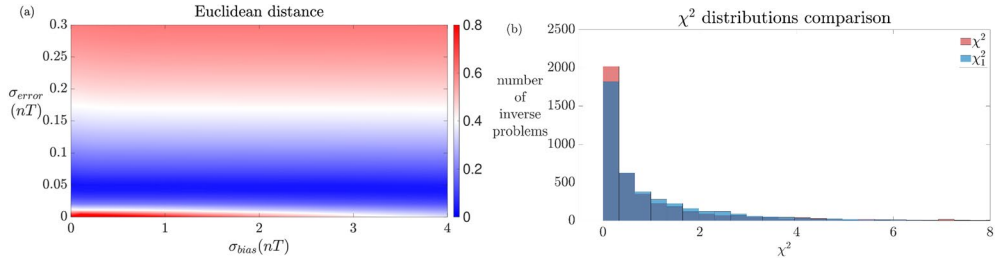

Figure 8. Choosing optimal values of σ_{bias} and σ_{error}. (a) Euclidean distance between the two normalized histograms of the calculated chi-square distribution and the theoretical degree 1 chi-square distribution as a function of σ_{bias} and σ_{error}. (b) Chi-square distribution obtained with (σ_{bias}, σ_{error}) equal to (0.25, 0.06) nT (in red) and reference chi-square distribution with 1 degree of freedom (in blue).

applying the prism method on all 4,176 prisms and calculating the chi-square for each prism. We obtain one distribution for each combination (σ_{bias}, σ_{error}) and compare it to a reference chi-square distribution of degree 1. The similarity between the two distributions is estimated by calculating the Euclidean distance between the two normalized histograms. The Euclidean distance is calculated by first normalizing both histograms and then taking the sum of the squared difference between the counts of each bin. This quantity ranges from 0 to 1.

Figure 8a presents the abovementioned Euclidean distance in the sampled two dimensional space. What is striking at first glance is that, although the standard deviation σ_{error} seems to be well constrained between 0.05 and 0.06 nT, there is a wide range of acceptable values for σ_{bias}. These values roughly lie between 0 and 1.8 nT. Here, we must remember that σ_{bias} characterizes the set of 18 biases that affect all 18 elements of the $\vec{R}$ vector from Section 3.2. Intriguingly, Figure 8 suggests that some sets of 18 biases with relatively high values could produce some errors of the same order of magnitude than the errors produced with relatively modest values. This observation suggests that in some configurations, the biases might cancel each other out through the calculation such that the current density estimate is not much affected.

According to Figure 8a, the value of 0.25 nT proposed in Section 4.2 lies within the region of acceptable values for σ_{bias}. We therefore keep this value and next set σ_{error} to 0.06 nT as this is approximately the value for which the minimum occurs. Figure 8b shows a comparison between the histogram of the chi-square distribution obtained with (σ_{bias}, σ_{error}) equal to (0.25, 0.06) nT and of a reference chi-square distribution with 1 degree of freedom. The two distributions are rather close, which confirms (0.25, 0.06) nT to be an appropriate choice. These values are used in the rest of this paper. Additionally, the choice of (0.25, 0.06) nT for (σ_{bias}, σ_{error}) also enables us to check the conditioning of the inverse problems for all 4,176 prisms, that is the conditioning of the matrices $\mathbf{G}^t\mathbf{V_j}\mathbf{D}^{-1}_{\mathbf{mod,j}}\mathbf{U}^t_{\mathbf{j}}\mathbf{G}$ in Equation 14. We find that the condition number of these matrices ranges from 2 to 270 and is on average 60, which is low enough for the matrices to be well-conditioned.

5. Tests Using Synthetic Data

The method presented in Section 3 is first applied to synthetic data on February 15, 2014. We use two different sets of synthetic data to validate our algorithm as well as to investigate the impact of some sources of error. In particular, a first set is produced using potential field models to investigate errors possibly associated with potential magnetic fields that might not have been properly removed during the preprocessing step (Section 2). A second set is produced using the TIE-GCM physics-based to both validate the algorithm in an ideal case and investigate the impact of the propagation of biases and errors that affect the magnetic data as described in Section 3.3.

5.1. Impact of Residual Potential Fields

In principle, the algorithm presented in Section 3 is only sensitive to the magnetic fields produced by currents flowing through the prisms. In theory indeed, the potential fields produced by geomagnetic sources located outside the prisms should result in zero currents. This is because the method relies on integration of

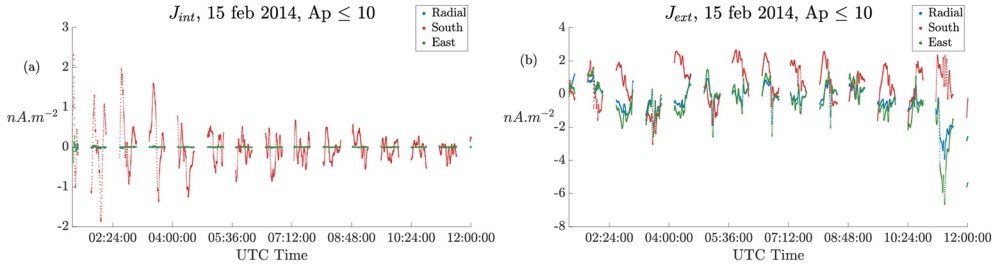

Figure 9. Radial (blue), south (red) and east (green) components of the $\vec{J}_{int}$ (a) and $\vec{J}_{ext}$ (b) current densities on February 15, 2014 and for quiet times.

the magnetic field on closed contours which, according to the Ampere theorem, takes nonzero values only when some currents flow through the surfaces defined by the contours. In practice, however, because the current density estimation relies on a finite number of points, we are forced to assume both linearity and stationarity of the magnetic field to approximate the contour integrals and solve the problem (Section 3.2). Yet potential fields are nonlinear and, for some of them, nonstationary. Despite the care taken in Section 2 to remove known potential fields in the Swarm vector data, some residual potential fields may remain in the magnetic data used in this study. This could then lead to artifact currents when using our method.

We performed a dedicated test to evaluate the impact of such residual potential fields on our results. We produced residual potential field synthetic data using five potential field models: the Comprehensive model (Section 2), the CHAOS-6-x9 extension of the CHAOS-6 model (Finlay et al., 2016), the MF7 version of the MF model series (Maus et al., 2008), the L2 Swarm product DIFI model (Chulliat et al., 2016) version 0402, and the POMME-10 version of the POMME model series (Maus et al., 2006). Here, our working assumption is that differences in the core, lithospheric, E-region ionospheric, and magnetospheric fields predicted by these models reflect any remaining potential fields in the magnetic data. Note that such an assumption necessarily has some limitations since these models do not represent the full spatiotemporal variation spectrum of potential fields. Nevertheless, we expect this test to give a sense of the magnitude of the impact of residual potential fields.

We consider internal (core and lithospheric) and external (E-region ionospheric and magnetospheric) fields separately. The first can be considered static over a few minutes, while the second may vary more substantially on this same time scale. For each prism, we compute a vector $\vec{R}_{int}$, similar to the vector $\vec{R}$ (Equation 3), defined as:

$$\vec{R}_{int} = \vec{B}^{CM}_{core} + \vec{B}^{CM}_{lith} - \vec{B}^{CHAOS}_{core} - \vec{B}^{MF7}_{lith} \tag{18}$$

where the subscript int stands for *internal*, $\vec{B}^{CM}_{core}$ and $\vec{B}^{CHAOS}_{core}$ are the magnetic field predictions of the core field by the Comprehensive and CHAOS-6-x9 models, and $\vec{B}^{CM}_{lith}$ and $\vec{B}^{MF7}_{lith}$ are the magnetic field predictions of the lithospheric field by the Comprehensive and MF7 models, all computed at the vertexes of the prism. Similarly, we compute a $\vec{R}_{ext}$ vector, now defined as:

$$\vec{R}_{ext} = \vec{B}^{CM}_{iono} + \vec{B}^{CM}_{magn} - \vec{B}^{DIFI}_{iono} - \vec{B}^{POMME10}_{magn} \tag{19}$$

where the subscript *ext* stands for *external*, $\vec{B}^{CM}_{iono}$ and $\vec{B}^{DIFI}_{iono}$ are the magnetic field predictions of the E-region ionospheric field by the Comprehensive and DIFI models, and $\vec{B}^{CM}_{magn}$ and $\vec{B}^{POMME10}_{magn}$ are the magnetic field predictions of the magnetospheric field by the Comprehensive and POMME-10 models. The vectors $\vec{R}_{int}$ and $\vec{R}_{ext}$ are then used as inputs to our method. Running separately $\vec{R}_{int}$ and $\vec{R}_{ext}$ in Equation 14 leads to the solutions $\vec{J}_{int}$ and $\vec{J}_{ext}$. In an ideal case, we would like $\vec{J}_{int}$ and $\vec{J}_{ext}$ to be zero. Any deviation from zero represents the spurious currents produced by nonlinear and nonstationary residual potential fields.

Figure 9 presents the current densities $\vec{J}_{int}$ on the left and $\vec{J}_{ext}$ on the right computed for all 4,176 prisms on February 15, 2014. Concerning $\vec{J}_{int}$, we observe that the radial and east components are close to zero whereas the south component can reach 2 nA.m^{-2}. Here, it is interesting to recall that $\vec{J}_{int}$ represents the

spurious currents produced by residual internal potential fields which are considered stationary over a few minutes. Therefore, in this case, deviations from zero are associated with nonlinear potential fields only. Interestingly, the south component seems to be the most impacted. Concerning $\vec{J}_{ext}$, we observe that all three components have similar magnitudes, reaching a maximum of 7 nA.m^{-2}. These $\vec{J}_{ext}$ represents the spurious currents produced by residual external potential fields, now both nonlinear and nonstationary. From these tests, we thus conclude that errors associated with nonlinear and nonstationary residual potential fields are of the order of several nA.m^{-2}, occasionally reaching up to 7 nA.m^{-2}.

5.2. Testing the Algorithm Using the TIE-GCM Model

The method is next tested using a second set of synthetic data produced with the Thermosphere Ionosphere Electrodynamics General Circulation Model (TIE-GCM) (Maute & Richmond, 2017a, 2017b; Qian et al., 2014). The TIE-GCM first solves for the electric potential of a static electric field in discretized flux tubes defined with the International Geomagnetic Reference Field IGRF-12 (Thébault et al., 2015). The electric field is then derived from the electric potential and the current is calculated with the requirement that the current divergence is null. The corresponding magnetic perturbation and current at a specific point in space can be calculated using a Poloidal-Toroidal spherical harmonic decomposition of the output current density grid (Alken et al., 2011; Engels & Olsen, 1998).

We use a TIE-GCM run for the fixed timestamp of February 15, 2009 12:00:00 UTC to produce the vector magnetic field predictions $\vec{R}_{tiegcm}$ at the vertexes of each prism and the vector current density predictions $\vec{J}_{tiegcm}$ at the center of inertia of the prisms. The $\vec{R}_{tiegcm}$ vector is similar to the $\vec{R}$ vector from Equation 3. Note that this vector does not contain errors nor biases and therefore represents ideal error-free measurements. It is also important to stress that all $\vec{R}$ vectors are computed at the same fixed timestamp. Therefore, it corresponds to an ideal case where all satellite magnetic data are synchronous, which is equivalent to consider a stationary F-region current system. Running $\vec{R}_{tiegcm}$ through Equation 14 leads to the solution $\vec{J}_{ideal}$ which represents a synthetic estimation of the uniform current inside the prisms.

5.2.1. Test Using Error-Free Synthetic Data

We first consider error-free synthetic data produced with the TIE-GCM model. We compare the recovered $\vec{J}_{ideal}$ currents to the current density predictions $\vec{J}_{tiegcm}$. Our goal here is to use the TIE-GCM model to perform an end-to-end test in order to validate the algorithm. In this section, even though all synthetic data are at the same timestamp, we will distinguish the prisms located in the morning sector (06:00–08:00 LT) to those located in the evening sector (18:00–20:00 LT) in the real configuration. Figures 10 and 11 present quasi-dipole latitudinal profile comparisons between the $\vec{J}_{ideal}$ and $\vec{J}_{tiegcm}$ currents for all three components and respectively in the morning and evening sectors. For each quasi-dipole latitudinal profile, a scale in nA.m^{-2} is given on the left side and the longitude of the equator crossing (ϕ_{eq}), the root mean square error (RMSE) and the Pearson correlation coefficient (C) are given on the right side.

Figures 10 and 11 show that the prism method does a very good job at recovering the current density on all three components. The RMSE does not exceed 0.1, 0.6, and 0.4 nA.m^{-2}, respectively on the radial, south, and east components, which means that the method introduces no significant bias. The correlation coefficient does not drop below 0.75 showing that the variability of the current is also well captured. We also note that, on all three components, the current density in the morning sector (Figure 10) has an intensity of a few nA.m^{-2} whereas the current density in the evening sector (Figure 11) seldom exceeds 1 nA.m^{-2}. Still, in both configurations, our method seems to perform equally well.

This synthetic test shows that our approach is a reliable technique to estimate current density in the F-region ionosphere. In the ideal case where the magnetic data at the vertexes of the prism are both error-free and synchronous, it provides estimates to within roughly 0.5 nA.m^{-2} when considering the Swarm constellation during February 15, 2014. These minor errors are of the same order of magnitude than the errors produced by nonlinear residual potential fields as described in Section 5.1 (Figure 9a). Based on this observation, it is our interpretation that these errors are associated with the slight nonlinearity of the currents and associated magnetic fields produced by the TIE-GCM model.

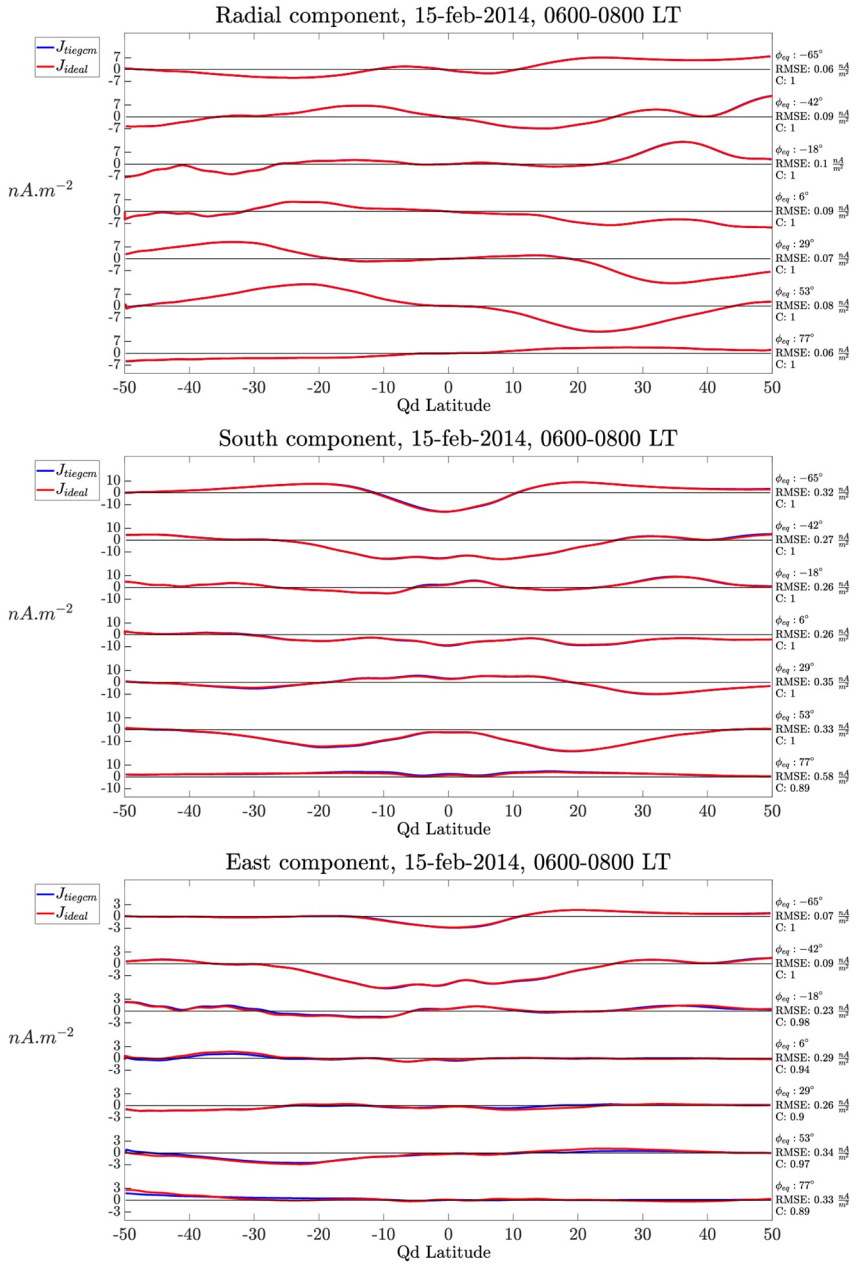

Figure 10. Quasi-dipole latitudinal profiles of the $\vec{J}_{tiegcm}$ (blue curves) and $\vec{J}_{ideal}$ (red curves) currents in the morning sector (06:00–08:00 LT) during quiet times on February 15, 2014. The radial, south, and east components are respectively displayed on the top, middle, and bottom panels. The longitude of the equator crossing (ϕ_{eq}), root mean square error (RMSE) and Pearson correlation coefficient (C) are given beside each profile on the right.

5.2.2. Impact of Errors and Biases

We now consider the impact of errors and slowly varying biases that affect the data as described in Section 3.3. We reproduce a similar synthetic test as in Section 5.2.1 using the same (18 × 1) data vector $\vec{R}_{tiegcm}$ to which we add a (18 × 1) vector $\vec{R}_{bias}$, which contains biases, and a (18 × 1) vector $\vec{R}_{error}$, which contains random errors. The resulting vector is called $\vec{R}_{pertu}$. Running $\vec{R}_{pertu}$ through Equation 14 leads to the solution $\vec{J}_{pertu}$, where the subscript *pertu* stands for *perturbed*. We compare the $\vec{J}_{tiegcm}$ current, predicted by the TIE-GCM model, to the $\vec{J}_{pertu}$ current calculated with synthetic data affected by biases and errors. The biases and errors are produced in the following way:

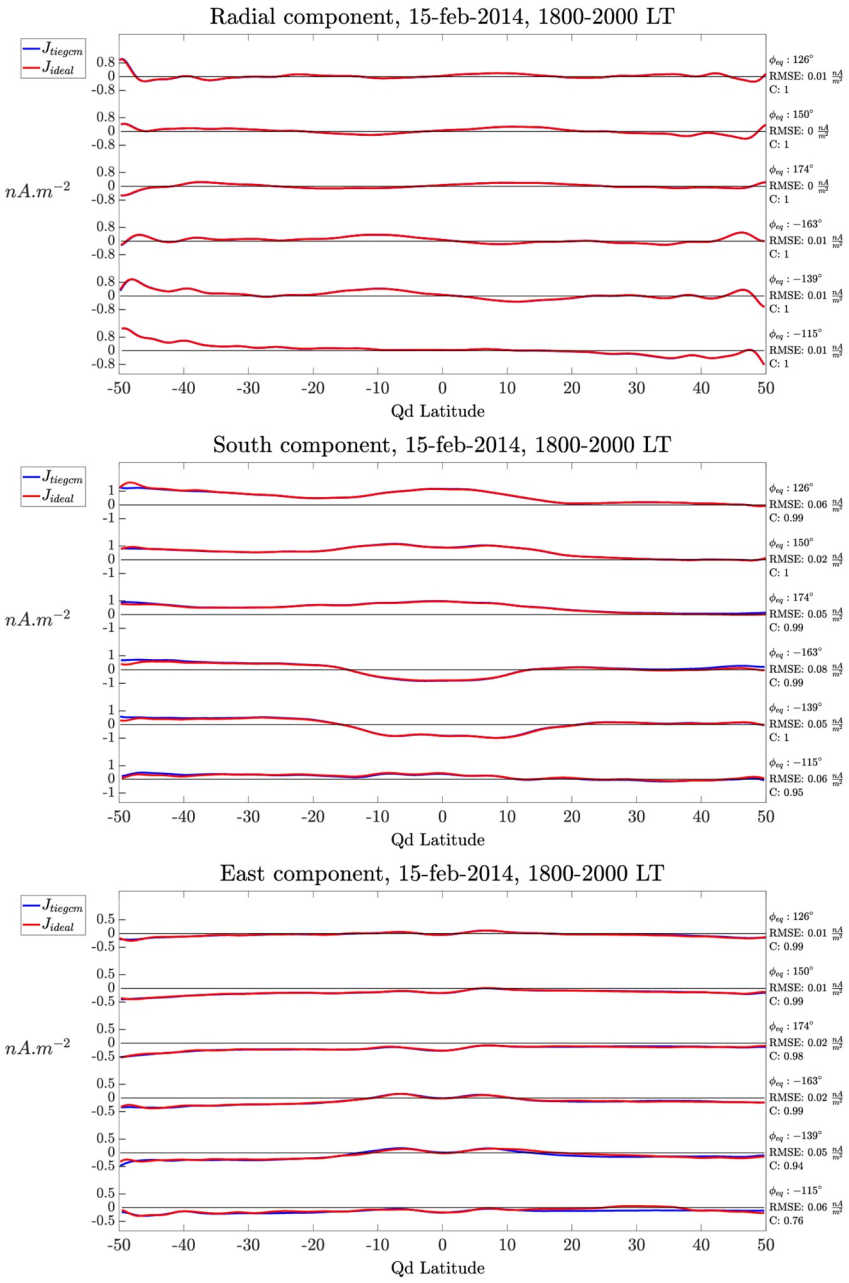

Figure 11. Same as Figure 10 in the evening sector (18:00–20:00 LT).

1. The elements of $\vec{R}_{bias}$ are generated using the Sun-disturbance empirical models used to correct the version 0505 Swarm vector data (Tøffner-Clausen et al., 2016). Our working assumption is that these dBSun models, whose predictions are provided together with the data, should reflect the temporal behavior of any remaining biases. The model predictions are rescaled in order to obtain biases of the same order of magnitude as what was observed in the scalar residuals (Section 4.2). On each of the three components of the dBSun correction, a scaling factor is applied such that the Euclidean distance from zero (Equation 15) of the rescaled dBSun is 0.25 nT (see again Section 4.2). This rescaled dBSun is used to produce time series of $\vec{R}_{bias}$ with realistic amplitude and time variations, consistent with our choice of σ_{bias} (Section 4.2).
2. The elements of $\vec{R}_{error}$ are independently generated using a random Gaussian process of mean 0 nT and SD 0.06 nT chosen according to Section 4.5.

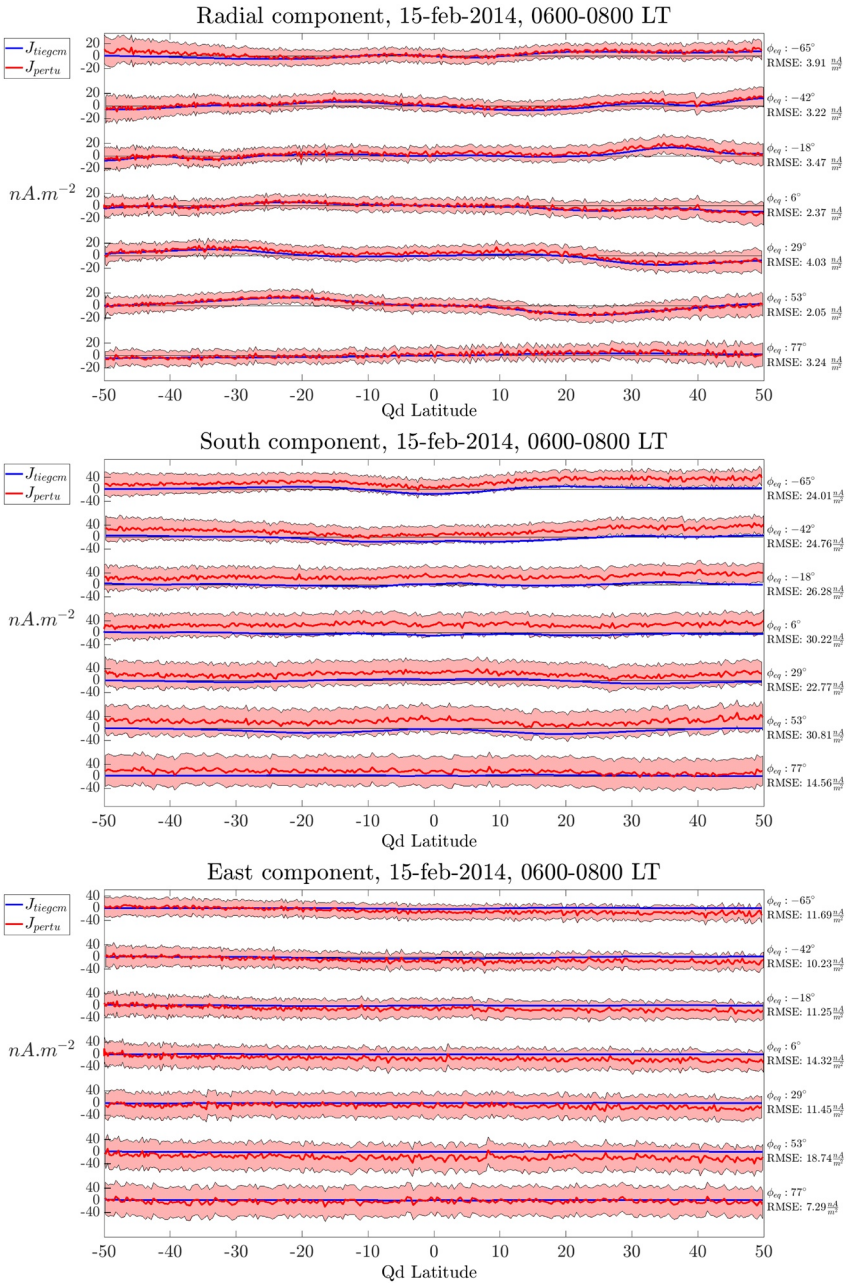

Figure 12. Quasi-dipole latitudinal profiles of the $\vec{J}_{tiegcm}$ (blue curves) and $\vec{J}_{pertu}$ (red curves) currents in the morning sector (06:00–08:00 LT) during quiet times on February 15, 2014. Top, middle and bottom panels display the radial, south and east components. The longitude of the equator crossing (ϕ_{eq}) and root mean square error (RMSE) are given on the right beside each profile. The red shaded areas are delimited by the $\pm 2\sigma_J$ curves around $\vec{J}_{pertu}$, where σ_J is taken from the diagonal elements of the a posteriori covariance matrix $\mathbf{C_J}$ (Equation 8).

Figures 12 and 13 present quasi-dipole latitude profiles of the $\vec{J}_{tiegcm}$ current and the $\vec{J}_{pertu}$ in the morning (06:00–08:00 LT) and evening (18:00–20:00 LT) sectors. The shaded red areas are delimited by the $\pm 2\sigma_J$ curves around $\vec{J}_{pertu}$, where σ_J is taken from the diagonal elements of the a posteriori covariance matrix $\mathbf{C_J}$ (Equation 8). A scale in nA.m^{-2} is given on the left beside each profile and the longitude of the geographic equator crossing (ϕ_{eq}) together with the root mean square error between $\vec{J}_{tiegcm}$ and $\vec{J}_{pertu}$ (RMSE) are given on the right side.

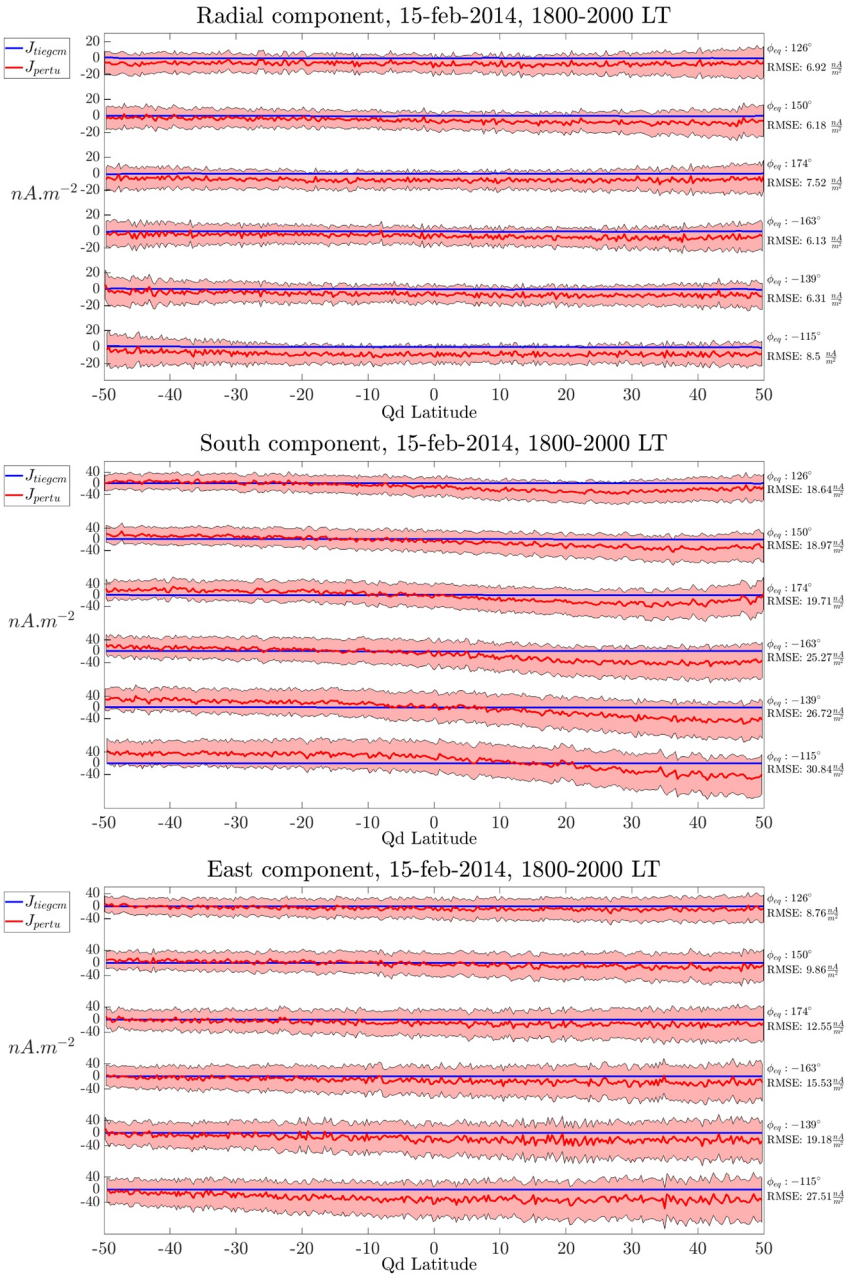

Figure 13. Same as Figure 12 in the evening sector (18:00–20:00 LT).

Looking at Figures 12 and 13, the RMSE values for each component range roughly from 2 to 9 nA.m^{-2} (radial), 14–32 nA.m^{-2} (south), and 7–28 nA.m^{-2} (east). These values exceed by far the 0.5 nA.m^{-2} error introduced by the method itself (Section 5.2.1). The error on $\vec{J}_{pertu}$ is mainly dominated by a slow-varying offset rather than by noise on all components. This slow-varying offset results from the propagation of the bias vector $\vec{R}_{bias}$ through the calculation. Because of its temporal structure, it can easily be mistaken for true ionospheric signals. Consequently, it is important to check if the error bars, represented by the red shaded areas in Figures 12 and 13, can be trusted. More specifically, we would like the $\vec{J}_{tiegcm}$ current—the current we are trying to recover—to be within these error bars at anytime.

On the radial component, in both the morning and evening sectors (top panels of Figures 12 and 13), the $\vec{J}_{tiegcm}$ currents always occur within or at the very limit of the error bars. One can reach a similar conclusion for the east component in both the morning and evening sectors and for the south component in the evening

sector. For the south component in the morning sector, however, the error bars turn out to be less reliable. Indeed, we observe that the $\vec{J}_{tiegcm}$ currents lie slightly outside the error bars in the northern hemisphere on the profiles corresponding to ϕ_{eq} equal to −18°, −42°, and −65°. The maximum discrepancy reaches 9 nA.m^{-2}. In conclusion, the error bars seem to be reliable everywhere on the radial and east component as well as on the south component in the evening sector. They are also reliable everywhere on the south component in the morning sector except for some tiny segments in the northern hemisphere.

6. Application to Swarm Data

We now turn to the current densities derived from real Swarm data. We first compare our results to the Level-2 FAC Swarm product (Ritter et al., 2013), which only provides one component of the current density. We then move on to illustrate and discuss the signals observed on the three components of the current density recovered with our algorithm.

6.1. Comparison With the Level-2 FAC Swarm Product

The Level-2 FAC Swarm product (Ritter et al., 2013) provides estimates of one component of the current density in the F-region ionosphere. It uses vector measurements of the Swarm satellites Alpha and Charlie. The measurements are first corrected for the core, lithospheric, and magnetospheric fields using, to the extent of our knowledge, the IGRF11 (Finlay et al., 2010), MF7, and POMME-6 models (Ritter et al., 2013). The corrected data are subsequently low-pass filtered. The current density is then estimated using successive data of Swarm Alpha and Charlie to form four-sided polygons and by applying the integral version of the curl-B technique to the polygons. This technique is similar to that used by our algorithm, which applies it to all five surfaces of the prisms. On the day of interest in this study, February 15, 2014, the Level-2 FAC Swarm product is only available for a little more than two hours. Recall also that on this day the Swarm constellation is in the configuration illustrated in Figure 2 where we can see that the plan formed by successive positions of the Swarm satellites Alpha and Charlie is not perpendicular to the local vertical. The Level-2 FAC Swarm product thus provides an estimate of the current density through this surface, to which we refer as the $AA'CC'$ surface.

We compare this current density, to which we refer as $j_{AA'CC'}L2$, to two quantities computed using our algorithm. First, the current density through this same surface directly computed with the curl-B technique of Section 3.2. This corresponds to the element of the $\vec{J}_p$ vector (Equation 3) associated with this surface. We note this quantity $j_{AA'CC'}$. Second, the recovered $\vec{J}$ vector (Equation 14) projected on the normal vector of the surface $AA'CC'$, which we note $J_{AA'CC'}$. This corresponds to the prediction of our current density model $\vec{J}$.

Figure 14 presents the results of the comparison on February 15, 2014 everywhere where there are data in common. $j_{AA'CC'}$ $L2$ is shown in black, $j_{AA'CC'}$ in green and $J_{AA'CC'}$ in red, all as a function of the quasi dipole latitude between ±50°. We first note an excellent agreement between $j_{AA'CC'}$ and $J_{AA'CC'}$. This shows that the $J_{AA'CC'}$ vector—recovered with our algorithm—fits very well the $j_{AA'CC'}$ component—one of the five elements of the $\vec{J}_p$ vector used to recover it. We also observe a good agreement between $j_{AA'CC'}$ $L2$ and both $j_{AA'CC'}$ and $J_{AA'CC'}$. In particular, all curves share a similar dynamics and disagreements usually lie within the predicted error bars. Sometimes, however, offsets can be seen between the Level-2 FAC Swarm product and our estimates. Although these offsets can reach up to 20 nA.m^{-2}, they are usually of the order of 5–10 nA.m^{-2}. This is typically the order of magnitude of artifacts produced by residual non-potential fields (Section 5.1) when different potential field models are used to preprocess the data, as is indeed the case here. We thus conclude that the results produced by our algorithm are consistent with the Level-2 FAC Swarm product.

6.2. Recovered Vector Current Density on February 15, 2014

We now turn to the interpretation of the signals observed on the three components of the current density recovered with our algorithm using real Swarm data. Similar to Figures 12 and 13, Figures 15 and 16 present quasi-dipole latitudinal profiles of the current density in the morning and evening sectors for geomagnetic quiet times and during February 15, 2014. On these figures, a scale in nA.m^{-2} is given beside each profile on the left and the longitude of the equator crossing on the right. The colored areas are delimited by the

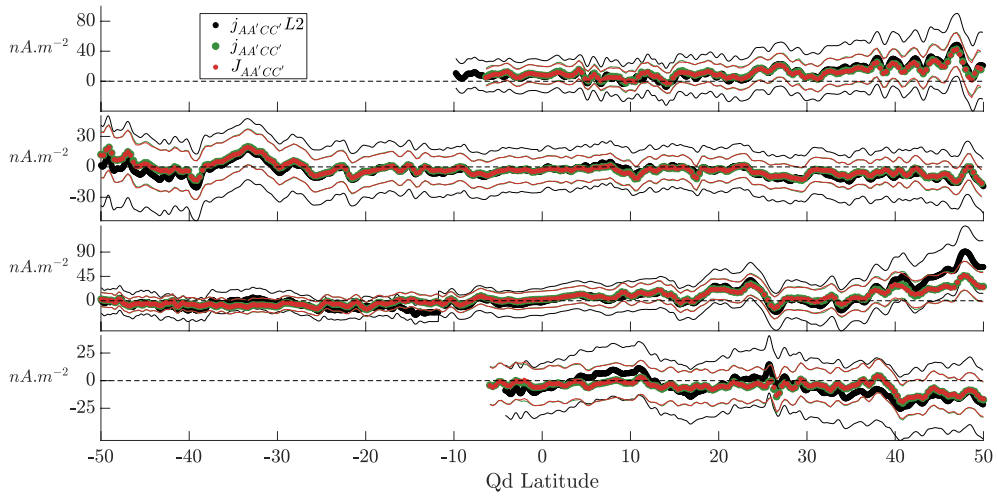

Figure 14. Comparison of quasi dipole latitudinal profiles of the current density through the surface AA′CC′ from the Level-2 FAC Swarm product ($j_{AA'CC'}$ L2, in black), the current density through the surface AA′CC′ computed with the integral version of the curl B technique by our algorithm ($j_{AA'CC'}$, in green) and the projection of the $\vec{J}$ current density model recovered with our algorithm on the normal vector of the surface AA′CC′ ($J_{AA'CC'}$, in red). For each curve, the corresponding error bars are shown in the same color.

$\pm 2\sigma_J$ curves where σ_J is taken from the diagonal elements of the $\mathbf{C_J}$ a posteriori covariance matrices from Equation 8. The black stars, labeled with numbers within parentheses, mark specific positions whose coordinates and current density components are given in Table 3 for profiles in the morning sector and Table 4 for profiles in the evening sector. These markers will help discuss the observed currents.

Due to the large error bars on the derived currents, it is not possible to give precise intensities. Rather, in the following sections we will focus on the physical origins of the currents whenever currents are detected, that is, when the currents and the error bars diverge distinctly from zero. We will propose various mechanisms to explain the observed signal in relation with the current understanding of the ionospheric F-region current system. As we are looking at only one day, our analysis will focus on very specific circumstances corresponding to geomagnetic quiet-time at low and mid quasi-dipole latitudes in the morning and evening sectors during the northern hemisphere winter. To ease the following discussion, we refer to a specific quasi-dipole latitudinal profile using the longitude of the equator crossing ϕ_{eq}.

6.2.1. Discussion of Interhemispheric Field-Aligned Currents

Interhemispheric field-aligned currents (IHFACs) have been widely studied for the past 40 years. Their existence was first predicted using numerical simulations (Fukushima, 1994; Maeda, 1974; Takeda, 1982) and was observationally confirmed by Olsen (1997). The latter, looked at the signature of IHFACs on the radial component of the poloidal current density at the altitude of the MAGSAT satellite derived from a spherical harmonic representation of the toroidal magnetic field. Because of the MAGSAT orbital configuration, he could only study these currents in the morning and evening sectors. Further studies using different methodologies and data set have extended our knowledge of IHFACs climatology. These include in particular Yamashita and Iyemori (2002) who looked at the IHFAC signature on the magnetic field east component measured by the Ørsted satellite in conjunction with the signature on the declination measured by ground observatories and Park et al. (2011) who studied IHFAC signature on the magnetic zonal component measured by the CHAMP satellite. These studies revealed important features of low-latitude IHFACs which were thought to flow from the summer to winter hemisphere in the morning sector and from the winter to summer hemisphere around noontime. They could not, however, grasp the full complexity of this current system. In particular, the direction of evening sector IHFACs remained unclear.

A new understanding of the IHFACs climatology recently emerged. Lühr et al. (2015), who used the curl-B technique to compute the radial current density at the Swarm satellite altitude, found summer to winter IHFACs around 16:00 LT during the June solstice and equinoxes. This result was confirmed by later studies

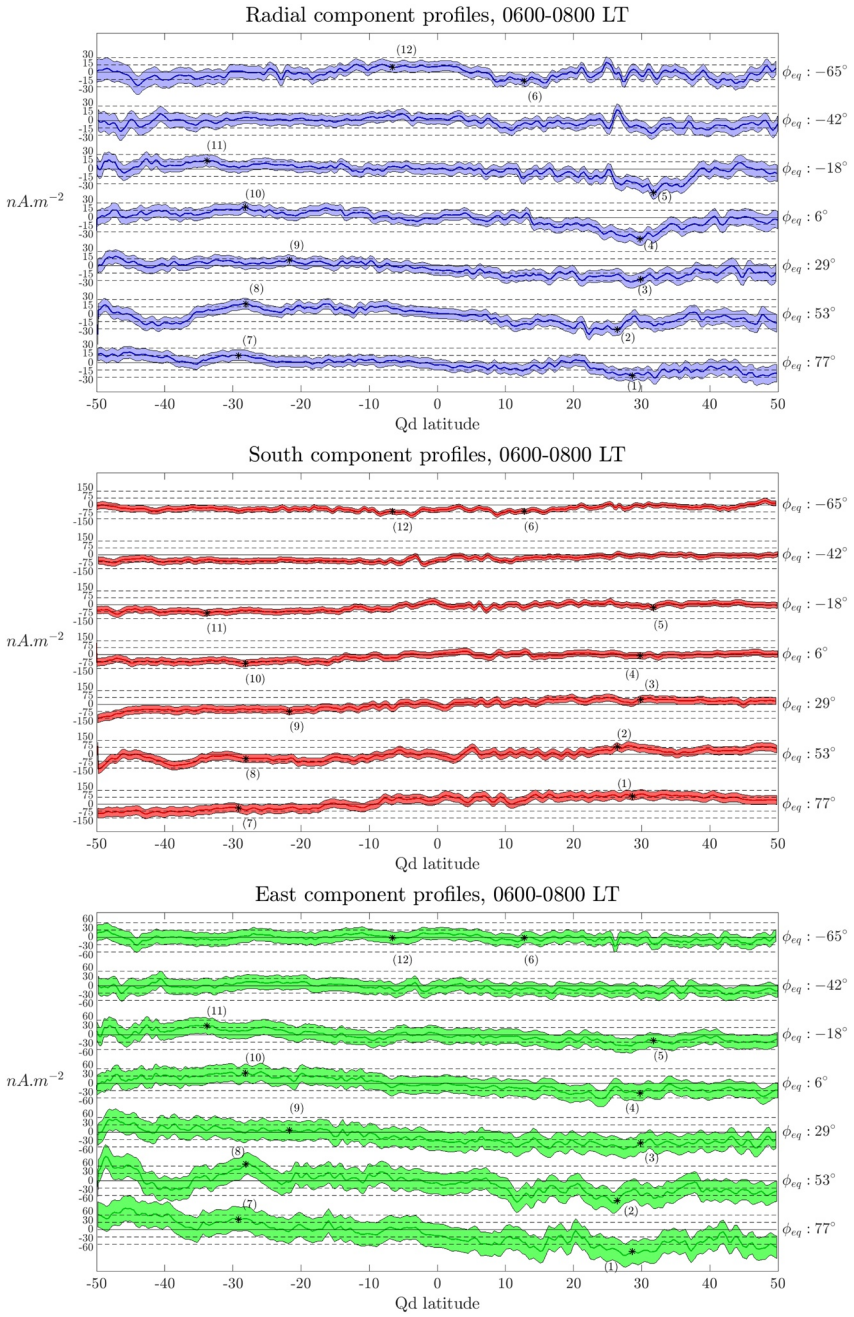

Figure 15. Quasi-dipole latitudinal profiles of the current density radial (top panel), south (middle panel), and east (bottom panel) component in the morning sector during February 15, 2014 and quiet times. The plain lines represent the derived currents and the colored areas the uncertainties. A scale in $nA.m^{-2}$ is given on the left of each profile and the longitude of the equator crossing (ϕ_{eq}) on the right. The black stars, labeled with numbers inside parentheses, mark the positions whose coordinates and current density components are given in Table 3.

(Fathy et al., 2019; Lühr et al., 2019; Park et al., 2020). Park et al. (2011) and Lühr et al. (2015) also reported longitudinal variations of low-latitude IHFACs originating from both longitudinal variations of the main field and a modulation by upward propagating atmospheric tides. Lühr et al. (2019) stressed that whereas the longitudinal structures of IHFACs during the June solstice and equinoxes are similar and consistent with the current knowledge, the December solstice longitudinal structure is more complicated. IHFACs also display a latitudinal dependency (Fathy et al., 2019; Park et al., 2011). In particular, Park et al. (2020) revealed that another IHFAC system above 35° of magnetic latitude flows in the opposite direction during

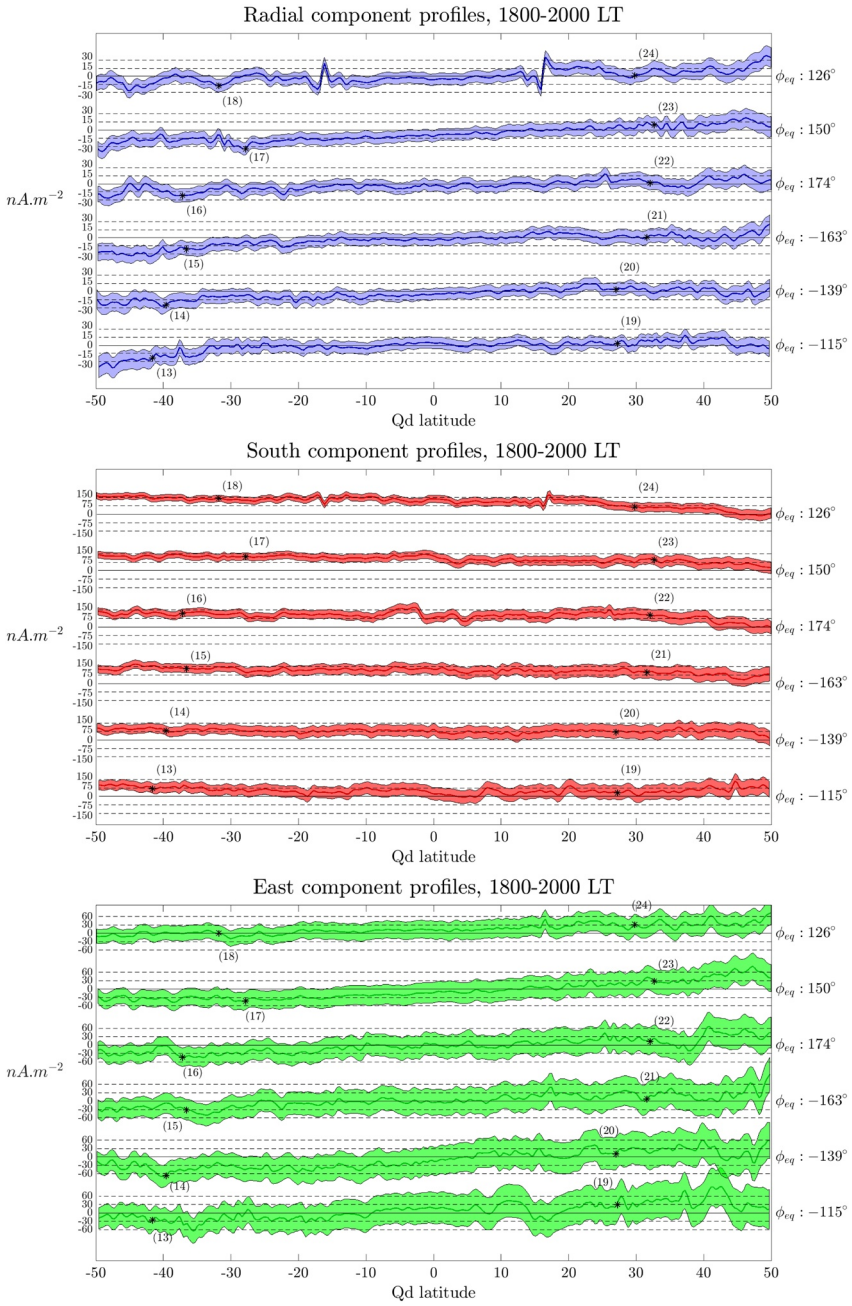

Figure 16. Same as Figure 15 in the evening sector. The corresponding table is Table 4.

June solstice and equinoxes. He terms the currents below 35° low-latitude IHFACs and those above 35° mid-latitude IHFACs. We will adopt the same terminology.

All these studies look at IHFAC signatures on one component of either the magnetic field or the current. Using the information in one direction only makes it difficult to disentangle contributions from IHFACs and other currents. Our algorithm provides the three components simultaneously and therefore an opportunity to better appreciate the relative intensities of all currents in the F region. Additionally, February 15, 2014 is a particularly interesting day as is it both during winter in the northern hemisphere, when the longitudinal variations of IHFACs display complicated structures, and at a time when the Swarm satellites orbit in the morning and evening local time sectors, where IHFACs are suspected or known to flow.

Table 3
Numerical Values of the Points Marked by a Black Star on Figure 15 Corresponding to the Morning Sector

Marker number[a]	Longitude (°)[b]	Qd latitude (°)[c]	Radial (nA.m^{-2})[d]	South (nA.m^{-2})[e]	East (nA.m^{-2})[f]
(1)	76.1	28.6	−26.3 ± 12.8	92.1 ± 49.2	−89 ± 48.1
(2)	52.5	26.4	−31 ± 12.5	85.3 ± 44.2	−80.7 ± 43.6
(3)	28.8	29.8	−27.1 ± 13.2	56.6 ± 39.5	−42.6 ± 38.3
(4)	5.1	30.1	−43.5 ± 13.4	−13.8 ± 35	−36.6 ± 33.4
(5)	−18.6	31.7	−48.8 ± 13.3	−30.6 ± 31.3	−23.4 ± 29.2
(6)	−65.5	12.7	−18 ± 10.7	−68.6 ± 25.7	−1.7 ± 23.8
(7)	77.1	−29.2	15.3 ± 11	−42.3 ± 49.4	−43.5 ± 49.6
(8)	53.4	−28.1	22 ± 11	−47.4 ± 45.6	70.3 ± 44.9
(9)	29.6	−21.7	12.6 ± 10.7	−73.8 ± 40.7	8.4 ± 39.8
(10)	6	−28.2	21.8 ± 11	−98.6 ± 36.9	43.9 ± 35.7
(11)	−17.5	−33.8	18.2 ± 12	−90.5 ± 34.2	36.3 ± 32.5
(12)	−65.1	−6.6	10.8 ± 11.1	−73.5 ± 26.3	−1.9 ± 24.3

[a]Marker number of markers displayed on Figure 15. [b]Marker longitude. [c]Marker quasi-dipole latitude. [d]Current density radial component with 2σ uncertainties. [e]Current density south component with 2σ uncertainties. [f]Current density east component with 2σ uncertainties.

6.2.1.1. *In the Morning Sector*

In the morning sector during winter in the northern hemisphere, IHFACs exhibit a strong longitudinal variability (Lühr et al., 2019). Depending on the longitude sector, they can either flow from summer to winter hemisphere or the other way around. Furthermore, whereas the existence of a low-latitude IHFACs is quite established, Park et al. (2020) could not see a clear signature of mid-latitude IHFACs in the morning local time sector investigated here.

In the top panel of Figure 15, downward currents are detected in the northern hemisphere morning sector on the profiles corresponding to ϕ_{eq} equal to 77°, 53°, 29°, 6°, and −18° at latitudes between 20° and 35°. Examples of numerical values for these currents, corresponding to markers (1), (2), (3), (4), and (5) on Figure 15, are given in Table 3. For instance, on the profiles ϕ_{eq} equal to 6° and −18°, markers (4) and (5) indicate downward currents of respectively −43.5 ± 13.4 and −48.8 ± 13.3 nA.m^{-2}. Such currents are likely to be associated with low-latitude IHFACs. Markers (2), (3), (4), and (5) are indeed located around the African

Table 4
Same as Table 3, but for the Points Marked on Figure 16 Corresponding to the Evening Sector

Marker number	Longitude (°)	Qd latitude (°)	Radial (nA.m^{-2})	South (nA.m^{-2})	East (nA.m^{-2})
(13)	−115.4	−41.6	−22.9 ± 16.3	71.7 ± 44.1	−24.3 ± 42.2
(14)	−139.3	−39.6	−24.8 ± 14.3	84.4 ± 41.2	−65.3 ± 39.7
(15)	−163.1	−36.6	−20.6 ± 12.8	133.9 ± 38.3	−30.5 ± 37
(16)	173.3	−37.2	−21 ± 12.4	122.3 ± 34.6	−42.6 ± 33.3
(17)	149.7	−27.9	−34.8 ± 11.3	126.4 ± 32.7	−41 ± 31.4
(18)	126	−31.8	−17.4 ± 11.4	140.6 ± 35.2	0.7 ± 27.3
(19)	−114.7	27.2	4.1 ± 11.3	34.2 ± 63.1	30.5 ± 62.9
(20)	−138.3	27	4.4 ± 11.7	73.3 ± 58.2	11.8 ± 57.8
(21)	−162	31.5	0.8 ± 12.7	101.6 ± 54.9	8.9 ± 53.9
(22)	174.3	32.1	2.2 ± 13.4	105.3 ± 50.2	14.7 ± 48.8
(23)	150.6	32.6	10.5 ± 13.8	97.4 ± 45.1	30.4 ± 43.3
(24)	127	29.8	1.5 ± 13.1	65.2 ± 38.9	31.6 ± 37

longitudinal sector (−20°–60°) where summer to winter currents—that is northward and downward in February—have been reported by Fathy et al. (2019) in the morning. We do not see, however, signatures of mid-latitude IHFACs in the northern hemisphere.

As the currents flow from one hemisphere to the other, a downward radial component in the northern hemisphere must be associated with an upward component in the southern hemisphere. Upward currents are indeed detected on the top panel of Figure 15 on the profiles corresponding to ϕ_{eq} equal 77°, 53°, 6° and −18°. Numerical values corresponding to markers (7), (8), (10), and (11) are given in Table 3. The signal seems to be weaker in the southern hemisphere compared to the northern hemisphere. For instance, while marker (4) indicates −43.5 ± 13.4 nA.m^{-2}, marker (10) only indicates 21.8 ± 11 nA.m^{-2}. This difference is somehow expected as there is no requirement for the radial component to be purely antisymmetric with respect to the magnetic equator because the satellites do not necessarily cross the same field line at conjugate points.

IHFAC variations with longitude are difficult to assess with our data set as we do not have the full longitudinal coverage. Contrary to the profiles corresponding to ϕ_{eq} equal 77°, 53°, 29°, 6°, and −18°, the profile corresponding to ϕ_{eq} equal −42° does not display signatures of IHFACs in either hemisphere. Additionally, the profile corresponding to ϕ_{eq} equal to −65° display only very weak downward/upward currents (around marker 6/12) in the northern/southern hemisphere close to the magnetic equator and mostly no currents between 20° and 35°, except around 35° in the northern hemisphere. Although further investigations are needed, this observation is consistent in terms of wavelength with the longitudinal variations reported by Lühr et al. (2019) during the northern hemisphere winter.

IHFACs flowing northward must also produce a negative south component. It is interesting to check if the radial and south components are consistent. Middle panel of Figure 15 presents the south component of the estimated current density in the morning sector. We start by looking at the southern hemisphere. A clear negative south component is observed in this hemisphere on all profiles which is mostly consistent with the previous interpretation of the radial component. For instance, marker (10) indicates a downward current of 21.8 ± 11 nA.m^{-2} and a northward current with a negative south component of −98.6 ± 36.9 nA.m^{-2}. Quite surprisingly, however, and despite larger error bars, the south component seems two or three times as large as the radial component on these profiles (see for instance markers 8, 9, 10, and 11 in Table 3). Furthermore, whereas the radial upward component seem well located between 20° and 35°, the negative south component extends to a wider latitude range. We also notice that whereas no currents were detected on the radial component in the southern hemisphere on the profile corresponding to ϕ_{eq} equal −42°, there is a clear negative south component.

Turning to the northern hemisphere, the south component on the profiles corresponding to ϕ_{eq} equal 6° and −18° exhibits no clear direction as indicated by markers (4), −13.8 ± 35 nA.m^{-2}, and (5), −30.6 ± 31.3 nA.m^{-2}. More oddly, the profiles corresponding to ϕ_{eq} equal 77°, 53°, and 29° show a positive south component. Indeed, markers (1), (2), and (3) have a south component of respectively 92.1 ± 49.2, 85.3 ± 44.2, and 56.6 ± 39.5 nA.m^{-2}. In terms of IHFACs, this suggests currents flowing in opposite directions in the two hemispheres. This is inconsistent with IHFACs flowing from one hemisphere to the other.

All the observations on the south component in both the northern and southern hemisphere suggest that, besides IHFAC, other phenomena are at work. They will be discussed in Section 6.2.2.

6.2.1.2. In the Evening Sector

The most recent studies suggest that IHFACs in the afternoon mostly flow around 16:00 LT during the northern hemisphere summer and equinox seasons. During the northern hemisphere winter, however, the occurrence of IHFACs in this local time sector is unclear. In our study, the Swarm satellites orbit between 18:00 and 20:00 LT on the evening side. Whether IHFACs flow in this sector is quite an open question. In their Figure 5, Lühr et al. (2019) show that on average only very weak currents flow in this local time sector during the December solstice period which in their study includes the month of February. This observation, however, does not exclude that IHFACs could flow on an event basis.

The top panel of Figure 16 presents profiles of the radial component of the current density in the evening sector during February 15, 2014. In the southern hemisphere, the radial component exhibit downward

currents on all profiles. For instance, marker (15) display a radial component of -20.6 ± 12.8 nA.m^{-2} and marker (17) a radial component of -34.8 ± 11.3 nA.m^{-2}. In the northern hemisphere, however, we see no clear upward currents as shown for instance by marker (21), 0.8 ± 12.7 nA.m^{-2}, and marker (23), 10.5 ± 13.8 nA.m^{-2}. It is a possibility that these upward currents exist but are below the detection limit of our method. The precision of our method is indeed severely limited by the slow-varying biases affecting the Swarm data (Section 5.2.2). Whether the downward currents observed in the southern hemisphere are IHFACs or not is therefore ambiguous.

The middle panel of Figure 16 presents profiles of the south component on February 15, 2014. This component shows significant southward currents on all profiles except the one corresponding to ϕ_{eq} equal to $-115°$ for which most of the signal is consistent with a zero value within the error bars. On the profiles corresponding to ϕ_{eq} equal to $-163°$ and 174°, markers (15) and (16), respectively display a south component of 133.9 ± 38.3 and 122.3 ± 34.6 nA.m^{-2}. Here, similar findings to what was found in the morning sector applies: the sign of the south component is consistent with IHFACs flowing from the winter to the summer hemisphere. However, it is surprisingly three to 10 times larger than the radial component. For instance, marker (18) has a radial component of -17.4 ± 11.4 nA.m^{-2} and a south component of 140.6 ± 35.2 nA.m^{-2}.

6.2.2. Discussion of the South Component

The south component exhibits relatively high values which, as shown in Section 6.2.1, cannot be uniquely explained by IHFACs. The signal on this component also varies rather slowly along the profiles. This signal could be a signature of a large-scale ionospheric current or an artifact produced by some slow-varying biases which were not taken into account in the estimation of the error bars. Additionally, other sources of error could be associated with non-stationary magnetic fields and residual potential fields as shown in Section 5.1. We explore these possibilities.

In their Figure 3, which represents the height integrated currents in both the E and F region, Maute and Richmond (2017b) reveal that winds in the F-region produce current vortexes similar to those in the E region. We cannot make a direct comparison of their results with ours as they only provide results of a simulation for September equinox conditions. However, their simulation shows us that this current system flows clockwise in one hemisphere and anticlockwise in the other. In particular, it would mainly flow along a north-south axis both in the morning and evening sectors. We thus expect this current system to produce a signature on the south component which would be of opposite sign in the two hemispheres.

Such a behavior is indeed observed in Figure 15 on the profiles corresponding to ϕ_{eq} equal to 77°, 53°, and 29° in the morning sector. For instance marker (3) located in the northern hemisphere have a south component of 56.6 ± 39.5 nA.m^{-2} and marker (9) in the southern hemisphere a south component of -73.8 ± 40.7 nA.m^{-2}. The other profiles in the morning sector only present a clear negative south component in the southern hemisphere and no clear positive south component in the northern hemisphere. It is possible that the signal in the northern hemisphere is below the detection limit of our method on these profiles. This statement will need further investigations. Meanwhile, we propose that dynamo currents could possibly be responsible of the observed signal on the south component in the morning sector.

Things look a bit different in the evening sector (middle panel of Figure 16). On all profiles, except for the profile corresponding to ϕ_{eq} equal to $-115°$, we see a clear positive south component in the two hemispheres. The intensity of the signal also seems to decrease in the northern hemisphere. For instance marker (18) located in the southern hemisphere have a south component of 140.6 ± 35.2 nA.m^{-2} and marker (24) in the northern hemisphere a south component of 65.2 ± 38.9 nA.m^{-2}. To the extent of our knowledge, these characteristics are not signatures of a specific current system but rather a superposition of multiple effects.

We identified four effects that could explain the observed signal in the evening sector. First, although we could not confirm their existence in this local time sector (Section 6.2.1.2), there could be a contribution from IHFACs. IHFACs flowing from the winter to the summer hemisphere would indeed produce a positive south component in both hemispheres. The second effect is associated with the intensity decrease in the northern hemisphere. This feature could be a signature of the F-region dynamo current vortexes discussed hereinabove. This current system in the evening sector would indeed produce a signature on the south component of opposite sign compare to the morning sector: positive in the southern hemisphere and negative in the northern hemisphere.

Although they probably contribute, neither IHFACs nor dynamo currents can fully explain the rather large intensity on the south component (roughly 50–150 nA.m^{-2}). It is actually rather unlikely that any natural current produces such an intense signal in the evening sector. This statement leads us to consider the two other effects: the current density estimates on the south component could be particularly affected by remaining slow varying biases and there could be contributions from spurious currents generated by non-stationary magnetic fields and residual potential fields. Concerning the first effect, it should be pointed out that the dBSun correction implemented on the 0505 data used in this study assumes that the perturbation only affects the VFM instrument (Tøffner-Clausen et al., 2016). However, it is now known that part of this perturbation also affects the ASM instrument (Vigneron & Hulot, 2019). This aspect will need further investigations. Concerning the second effect, our method does not take into account errors generated by non-stationary magnetic fields and residual potential fields which can produce artifact offset up to 20 nA.m^{-2}. In the future, taking these errors into account will also be important to better characterize F-region currents.

6.2.3. Discussion of the East Component

F-region currents flowing in the east-west direction can be of several kinds. There could be contributions from gravity currents, pressure currents, wind-driven currents and currents driven by daytime/nighttime eastward/westward polarization electric field (Lühr et al., 2016). Lühr et al. (2016) computed the zonal current density in the F region using the curl-B technique and found currents up to roughly 40 nA.m^{-2}. By computing approximate current density intensity for each contribution using realistic values of the relevant physical quantities, they concluded that the sum of all contributions is in good agreement with their results. They also found quite large uncertainties, about 30 nA.m^{-2}, using similar considerations as we did. Numerical simulations, on their part, predict weaker zonal currents peaking at 5 nA.m^{2} at 400 km of altitude (Maute & Richmond, 2017b). We will analyze the east component derived with our method in light of all these considerations.

The east component in the bottom panels of Figures 15 and 16 displays large error bars making it difficult to provide a reliable physical interpretation of most of the derived signal. The east component derived with our method is more in line with the 40 nA.m^{2} of Lühr et al. (2016) than with the 5 nA.m^{2} of Maute and Richmond (2017b) (see the last columns of Tables 3 and 4). Our error bars are also consistent with the 30 nA.m^{-2} uncertainty of Lühr et al. (2016). This discrepancy between the F-region zonal currents calculated with numerical simulations and estimated with satellite data was previously noted by Maute and Richmond (2017b). Our results confirm it. Interestingly, most of the signal is consistent with a zero value within the error bars and as we showed in Section 5.2.2 the errors are mostly due to the slow-varying biases. We therefore propose that part of the discrepancy between numerical simulation predictions and the zonal currents derived with Swarm data is caused by the slow-varying biases affecting the Swarm data.

We now discuss the detected currents although these currents lie very close to the detection limit of our method. In the morning sector (Figure 15, bottom panel), westward currents are detected in the northern hemisphere on the profiles corresponding to ϕ_{eq} equal to 77°, 53°, 29°, 6°, and −18°. The most significant detections are marked by markers (1) and (2) which have an east component of -89 ± 48.1 and -80.7 ± 43.6 nA.m^{-2}. In terms of physical drivers, the F-region dynamo current system mentioned in Section 6.2.2 should not exhibit a significant eastward component in the dawn and dusk sectors. It can be safely ruled out. It is also difficult to predict what would be the currents produced by meridional winds (Lühr et al., 2016) and large scale polarization electric fields (Kelley, 2009) in these sectors. Although they have a clear behavior on the day and night side, the morning and evening sectors correspond to transition phases between the day and night configurations.

Gravity and pressure currents, however, could likely contribute. They flow in the same direction below the F2-layer plasma density peak whereas they cancel each other out above it (Alken et al., 2017; Maute & Richmond, 2017a). Gravity currents always flow eastward in the F region and therefore cannot explain our westward signal. In contrast, pressure currents could. Similarly to Section 6.2.2, we do not exclude that remaining slow-varying biases, non-stationary magnetic fields and residual potential fields could affect our

estimates therefore resulting in abnormally high current density. All these aspects will need further investigations which are beyond the scope of this study.

7. Conclusion

In this work, we presented the full algorithm of a new multispacecraft approach which provides estimates of the current density in the low- and mid-latitude the F-region ionosphere at the Swarm satellite altitude. The current density is estimated inside triangular prisms formed with successive positions of the three satellites of the Swarm constellation. This approach presents the advantage of being mostly sensitive to currents inside the prisms and allows for a study of the local current density in the F region.

We chose to work on a reduced data set. We used data from one day, February 15, 2014, because during this day the Swarm constellation was in an optimal configuration. We also only looked at geomagnetically quiet times, defined with the Ap index being less than 10, which reduced our data set to data before 1 pm. The algorithm was first tested on synthetic Swarm data. We first assessed the impact of residual potential fields. It was found that these residual fields can produce spurious currents up to nearly 10 $nA.m^{-2}$. We next validated the algorithm using synthetic data produced with the TIE-GCM model. It was shown that our algorithm provides accurate current density estimates to within 0.5 $nA.m^{-2}$ for an ideal case in which magnetic data are error-free and synchronous. These synthetic data were also used to highlight that biases and errors on the magnetic data can produce significant perturbations on the current density estimates. In particular, the slow varying biases turned out to be a severe limitation and prevented us from providing accurate current intensities. Because of this effect, we stress that one must exercise caution whenever such techniques are used to estimate the current density in the ionosphere.

Our algorithm was then applied to real Swarm data. We first checked that our algorithm leads to results consistent with the Level-2 FAC Swarm product, which unlike our approach only provides one component of the current density. We then took advantage of the three components of the current density recovered by our algorithm to discuss the signals observed on February 15, 2014. On this day, the three Swarm satellites span the morning (06:00–08:00 LT) and evening (18:00–20:00 LT) local time sectors. Signatures of interhemispheric field-aligned currents in the radial component were identified in the morning sector. Possible weaker signatures of these currents were identified in the evening sector. Additionally, we might have identified for the first time signatures in the south component of a specific F-region dynamo current system consisting of two vortexes rotating in opposite direction in both local time sectors. This aspect needs further investigations to make sure that the observed signal is not an artifact. Indeed, spurious current can be produced by propagation of errors and biases affecting the Swarm data through the computation or by nonlinear and nonstationary magnetic fields. As for the east component, the large error bars make the interpretation difficult. Nevertheless, we might have identified signatures of pressure currents in the morning sector though this will need to be confirmed.

It is planned to extend this study to as many days and local times as possible. Because the algorithm provides accurate estimates of the current density together with reliable uncertainties, we believe it has an interesting potential to study dynamical features in the low- and mid-latitude F-region ionosphere through event studies. It is, however, severely limited by the slow-varying biases affecting the Swarm data. In the future, an improved correction of these biases will hopefully allow us to take full advantage of this approach and to observe currents with intensities as little as 10 $nA.m^{-2}$. The approach could also be useful for future post-Swarm satellite missions.

Appendix A: Details on the Method Algorithm

This appendix focuses on giving the full details of Equations 3, 4, and 6 for which all terms will be written down. Here again, because the same formalism applies to all the prisms, we will only consider one prism such as the one presented in Figure 4. The letters α, β, and γ refer to the Swarm satellites Alpha, Bravo, and Charlie and we use no superscript to refer to the satellites at their initial positions and the prime superscript to refer to the same satellites at their positions 5 s later.

A1. Building of the $\vec{R}$ Vector and C_R Matrix

The $\mathbf{C_R}$ matrix is the covariance matrix associated with the magnetic data vector $\vec{R}$. Both these quantities were introduced in Sections 3.2 and 3.3. The (18×1) $\vec{R}$ vector is built by stacking the six vectorial magnetic data located at the vertexes of the prism:

$$\vec{R} = \begin{pmatrix} \boldsymbol{R_\alpha} \\ \boldsymbol{R_\beta} \\ \boldsymbol{R_\gamma} \\ \boldsymbol{R_{\alpha'}} \\ \boldsymbol{R_{\beta'}} \\ \boldsymbol{R_{\gamma'}} \end{pmatrix} \quad \text{with} \quad \boldsymbol{R_q} = \begin{pmatrix} R_q^x \\ R_q^y \\ R_q^z \end{pmatrix} \quad \text{and} \quad q = \{\alpha, \beta, \gamma, \alpha', \beta', \gamma'\}$$

where R_q^x, R_q^y et R_q^z are the Cartesian components of the magnetic vector data q in the Earth Centered Earth Fixed (ECEF) frame and q takes values inside $\{\alpha, \beta, \gamma, \alpha', \beta', \gamma'\}$. As discussed in Section 3.3, each element of this vector is affected by a bias and a random error and both can be treated as the result of Gaussian random processes. The bias on one Cartesian component is assumed to be constant over the 5 s that separate two measurements from the same satellite. This in turn introduces a correlation between the errors on two elements of the $\vec{R}$ vector which share the same bias. Taking into account these considerations, one can build the following covariance matrix $\mathbf{C_R}$ associated to the vector $\vec{R}$:

$$\boldsymbol{C_R} = \begin{pmatrix} \boldsymbol{C_\alpha} & \mathbf{0} & \mathbf{0} & \boldsymbol{C_{\alpha\alpha'}} & \mathbf{0} & \mathbf{0} \\ \mathbf{0} & \boldsymbol{C_\beta} & \mathbf{0} & \mathbf{0} & \boldsymbol{C_{\beta\beta'}} & \mathbf{0} \\ \mathbf{0} & \mathbf{0} & \boldsymbol{C_\gamma} & \mathbf{0} & \mathbf{0} & \boldsymbol{C_{\gamma\gamma'}} \\ \boldsymbol{C_{\alpha\alpha'}} & \mathbf{0} & \mathbf{0} & \boldsymbol{C_{\alpha'}} & \mathbf{0} & \mathbf{0} \\ \mathbf{0} & \boldsymbol{C_{\beta\beta'}} & \mathbf{0} & \mathbf{0} & \boldsymbol{C_{\beta'}} & \mathbf{0} \\ \mathbf{0} & \mathbf{0} & \boldsymbol{C_{\gamma\gamma'}} & \mathbf{0} & \mathbf{0} & \boldsymbol{C_{\gamma'}} \end{pmatrix}$$

$$\text{with} \quad \boldsymbol{C_q} = \begin{pmatrix} \sigma_{bias}^2 + \sigma_{error}^2 & 0 & 0 \\ 0 & \sigma_{bias}^2 + \sigma_{error}^2 & 0 \\ 0 & 0 & \sigma_{bias}^2 + \sigma_{error}^2 \end{pmatrix}$$

and

$$\boldsymbol{C_{qp}} = \begin{pmatrix} \sigma_{bias}^2 & 0 & 0 \\ 0 & \sigma_{bias}^2 & 0 \\ 0 & 0 & \sigma_{bias}^2 \end{pmatrix}$$

where σ_{bias} and σ_{error} are the SDs, respectively associated with the bias and the random error and are taken to be constant within the $\mathbf{C_R}$ matrix. The index q takes values inside $\{\alpha, \beta, \gamma, \alpha', \beta', \gamma'\}$ and p inside $\{\alpha', \beta', \gamma'\}$.

A2. Calculation of the $\vec{J_p}$ Vector and Error Propagation

The $\vec{J}_p$ vector, which was introduced in Section 3.2, is the (5×1) vector which contains the current density which flows through each of the five surfaces of one prism. This vector is calculated with Equation 3 which links the $\vec{R}$ vector to the $\vec{J}_p$ vector through the linear map $\mathbf{G_j}$. For the sake of clarity, we will decompose this calculation in two steps. The first step involves the projection of the magnetic data $\vec{R}$ located at the vertexes of the prism on its sides and with respect to the direction of integration for each surface of the prism. Writing these operations with matrices gives:

$$\vec{R}_{proj} = \boldsymbol{G_{proj}} \vec{R} \tag{A1}$$

where $\vec{R}_{proj}$ is a (18×1) vector such that:

$$\vec{R}_{proj} = \begin{pmatrix} \boldsymbol{R}^{\alpha}_{\boldsymbol{proj}} \\ \boldsymbol{R}^{\beta}_{\boldsymbol{proj}} \\ \boldsymbol{R}^{\gamma}_{\boldsymbol{proj}} \\ \boldsymbol{R}^{\alpha'}_{\boldsymbol{proj}} \\ \boldsymbol{R}^{\beta'}_{\boldsymbol{proj}} \\ \boldsymbol{R}^{\gamma'}_{\boldsymbol{proj}} \end{pmatrix}$$

with

$$\boldsymbol{R}^{\alpha}_{\boldsymbol{proj}} = \begin{pmatrix} R^{\alpha}_{\beta\alpha} \\ R^{\alpha}_{\alpha\gamma} \\ R^{\alpha}_{\alpha'\alpha} \end{pmatrix}, \boldsymbol{R}^{\beta}_{\boldsymbol{proj}} = \begin{pmatrix} R^{\beta}_{\beta\alpha} \\ R^{\beta}_{\gamma\beta} \\ R^{\beta}_{\beta'\beta} \end{pmatrix}, \quad \boldsymbol{R}^{\gamma}_{\boldsymbol{proj}} = \begin{pmatrix} R^{\gamma}_{\gamma\beta} \\ R^{\gamma}_{\alpha\gamma} \\ R^{\gamma}_{\gamma\gamma'} \end{pmatrix},$$

$$\boldsymbol{R}^{\alpha'}_{\boldsymbol{proj}} = \begin{pmatrix} R^{\alpha'}_{\alpha'\beta'} \\ R^{\alpha'}_{\gamma'\alpha'} \\ R^{\alpha'}_{\alpha'\alpha} \end{pmatrix}, \boldsymbol{R}^{\beta'}_{\boldsymbol{proj}} = \begin{pmatrix} R^{\beta'}_{\alpha'\beta'} \\ R^{\beta'}_{\beta'\gamma'} \\ R^{\beta'}_{\beta'\beta} \end{pmatrix} \text{et } \boldsymbol{R}^{\gamma'}_{\boldsymbol{proj}} = \begin{pmatrix} R^{\gamma'}_{\gamma'\alpha'} \\ R^{\gamma'}_{\beta'\gamma'} \\ R^{\gamma'}_{\gamma\gamma'} \end{pmatrix}$$

where each element R^{p}_{pq}, q and p taking values inside $\{\alpha, \beta, \gamma, \alpha', \beta', \gamma'\}$, is the magnetic data from the satellite p projected on the segment pq (see Figure 4) in the direction going from p to q. The matrix G_{proj} is the matrix that maps the vector $\vec{R}$ to $\vec{R}_{proj}$. Its full expression is:

$$\mathbf{G_{proj}} = \begin{pmatrix} \mathbf{U_{\alpha}} & \mathbf{0} & \mathbf{0} & \mathbf{0} & \mathbf{0} & \mathbf{0} \\ \mathbf{0} & \mathbf{U_{\beta}} & \mathbf{0} & \mathbf{0} & \mathbf{0} & \mathbf{0} \\ \mathbf{0} & \mathbf{0} & \mathbf{U_{\gamma}} & \mathbf{0} & \mathbf{0} & \mathbf{0} \\ \mathbf{0} & \mathbf{0} & \mathbf{0} & \mathbf{U_{\alpha'}} & \mathbf{0} & \mathbf{0} \\ \mathbf{0} & \mathbf{0} & \mathbf{0} & \mathbf{0} & \mathbf{U_{\beta'}} & \mathbf{0} \\ \mathbf{0} & \mathbf{0} & \mathbf{0} & \mathbf{0} & \mathbf{0} & \mathbf{U_{\gamma'}} \end{pmatrix}$$

with

$$\mathbf{U_{\alpha}} = \begin{pmatrix} u^{x}_{\beta\alpha} & u^{y}_{\beta\alpha} & u^{z}_{\beta\alpha} \\ u^{x}_{\alpha\gamma} & u^{y}_{\alpha\gamma} & u^{z}_{\alpha\gamma} \\ u^{x}_{\alpha'\alpha} & u^{y}_{\alpha'\alpha} & u^{z}_{\alpha'\boldsymbol{\alpha}} \end{pmatrix}, \mathbf{U_{\beta}} = \begin{pmatrix} u^{x}_{\beta\alpha} & u^{y}_{\beta\alpha} & u^{z}_{\beta\alpha} \\ u^{x}_{\gamma\beta} & u^{y}_{\gamma\beta} & u^{z}_{\gamma\beta} \\ u^{x}_{\beta'\beta} & u^{y}_{\beta'\beta} & u^{z}_{\beta'\beta} \end{pmatrix}, \mathbf{U_{\gamma}} = \begin{pmatrix} u^{x}_{\gamma\beta} & u^{y}_{\gamma\beta} & u^{z}_{\gamma\beta} \\ u^{x}_{\alpha\gamma} & u^{y}_{\alpha\gamma} & u^{z}_{\alpha\gamma} \\ u^{x}_{\gamma\gamma'} & u^{y}_{\gamma\gamma'} & u^{z}_{\gamma\gamma'} \end{pmatrix},$$

$$\mathbf{U_{\alpha'}} = \begin{pmatrix} u^{x}_{\alpha'\beta'} & u^{y}_{\alpha'\beta'} & u^{z}_{\alpha'\beta'} \\ u^{x}_{\gamma'\alpha'} & u^{y}_{\gamma'\alpha'} & u^{z}_{\gamma'\alpha'} \\ u^{x}_{\alpha'\alpha} & u^{y}_{\alpha'\alpha} & u^{z}_{\alpha'\alpha} \end{pmatrix}, \mathbf{U_{\beta'}} = \begin{pmatrix} u^{x}_{\alpha'\beta'} & u^{y}_{\alpha'\beta'} & u^{z}_{\alpha'\beta'} \\ u^{x}_{\beta'\gamma'} & u^{y}_{\beta'\gamma'} & u^{z}_{\beta'\gamma'} \\ u^{x}_{\beta'\beta} & u^{y}_{\beta'\beta} & u^{z}_{\beta'\beta} \end{pmatrix} \text{and } \mathbf{U_{\gamma'}} = \begin{pmatrix} u^{x}_{\gamma'\alpha'} & u^{y}_{\gamma'\alpha'} & u^{z}_{\gamma'\alpha'} \\ u^{x}_{\beta'\gamma'} & u^{y}_{\beta'\gamma'} & u^{z}_{\beta'\gamma'} \\ u^{x}_{\gamma\gamma'} & u^{y}_{\gamma\gamma'} & u^{z}_{\gamma\gamma'} \end{pmatrix}$$

where u^{x}_{pq}, u^{y}_{pq} et u^{z}_{pq} are the Cartesian coordinates in the ECEF frame of the unit vectors $\vec{u}_{pq}$ oriented in the direction of the segment pq from p to q.

The second step consists of performing the contour integral on each surface of the prism. The $\vec{R}_{proj}$ vector is mapped to the $\vec{J}_p$ vector through the relation:

$$\vec{J}_p = \boldsymbol{G_{curl}} \vec{R}_{proj} \tag{A2}$$

where $\boldsymbol{G_{curl}}$ full expression is:

$$\boldsymbol{G_{curl}} = \frac{1}{2\mu_0}\begin{pmatrix} \boldsymbol{Dl_1} \\ \boldsymbol{Dl_2} \\ \boldsymbol{Dl_3} \\ \boldsymbol{Dl_4} \\ \boldsymbol{Dl_5} \end{pmatrix}$$

with

$$\boldsymbol{Dl_1} = \frac{1}{S_1}\left(dl_{\beta\alpha}\ dl_{\boldsymbol{\alpha\gamma}}\ 0\ dl_{\beta\alpha}\ dl_{\gamma\beta}\ 0\ dl_{\gamma\beta}\ dl_{\alpha\gamma}\ 0\ 0\ 0\ 0\ 0\ 0\ 0\ 0\ 0\right)$$

$$\boldsymbol{Dl_2} = \frac{1}{S_2}\left(0\ 0\ 0\ 0\ 0\ 0\ 0\ 0\ 0\ dl_{\alpha'\beta'}\ dl_{\gamma'\alpha'}\ 0\ dl_{\alpha'\beta'}\ dl_{\beta'\gamma'}\ 0\ dl_{\gamma'\alpha'}\ dl_{\beta'\gamma'}\ 0\right)$$

$$\boldsymbol{Dl_3} = \frac{1}{S_3}\left(0\ 0\ 0\ 0\ -dl_{\gamma\beta}\ dl_{\beta'\beta}\ -dl_{\boldsymbol{\gamma\beta}}\ 0\ dl_{\gamma\gamma'}\ 0\ 0\ 0\ 0\ -dl_{\beta'\gamma'}\ dl_{\beta'\beta}\ 0\ -dl_{\beta'\gamma'}\ dl_{\gamma\gamma'}\right)$$

$$\boldsymbol{Dl_4} = \frac{1}{S_4}\left(-dl_{\beta\alpha}\ 0\ dl_{\alpha'\alpha}\ -\boldsymbol{dl}_{\beta\alpha}\ 0\ -dl_{\beta'\beta}\ 0\ 0\ 0\ -dl_{\alpha'\beta'}\ 0\ dl_{\alpha'\alpha}\ -dl_{\alpha'\beta'}\ 0\ -dl_{\beta'\beta}\ 0\ 0\ 0\right)$$

$$\boldsymbol{Dl_5} = \frac{1}{S_5}\left(0\ -dl_{\boldsymbol{\alpha\gamma}}\ -dl_{\alpha'\alpha}\ 0\ 0\ 0\ -dl_{\alpha\gamma}\ -dl_{\gamma\gamma'}\ 0\ -dl_{\gamma'\alpha'}\ -dl_{\alpha'\alpha}\ 0\ 0\ 0\ -dl_{\gamma'\alpha'}\ 0\ -dl_{\gamma\gamma'}\right)$$

where the indices going from 1 to 5 refer to the five surfaces of the prism, dl_{pq} is the length of the segment pq, p, and q still taking values in $\{\alpha, \beta, \gamma, \alpha', \beta', \gamma'\}$ and μ_0 is the vacuum permeability. The vector $\vec{J}_p$ can be written as:

$$\vec{J}_p = \begin{pmatrix} j_{p1} \\ j_{p2} \\ j_{p3} \\ j_{p4} \\ j_{p5} \end{pmatrix}$$

We finally return to Equation 3 in which the operator $\boldsymbol{G_j}$ maps $\vec{R}$ to $\vec{J}_p$ and is defined as:

$$\boldsymbol{G_j} = \boldsymbol{G_{curl}}\boldsymbol{G_{proj}} \tag{A3}$$

A3. Definition of the G Operator

Figure 4 illustrates the configuration of the forward problem defined in Equation 6. In the considered prism flows a current density $\vec{J}$ which is assumed to be a uniform field. We define on each surface a normal vector $\vec{n}_i, i$ ranging between 1 and 5 and referring to the surface number. The forward problem in Equation 6 links the current density $\vec{J}_p$, whose elements j_{pi} are the current density through surface i calculated with the curl-B technique, to the projection of the uniform field $\vec{J}$ on the normal vectors $\vec{n}_i$. The operator **G** is defined as:

$$G = \begin{pmatrix} n_{x,1} & n_{y,1} & n_{z,1} \\ n_{x,2} & n_{y,2} & n_{z,2} \\ n_{x,3} & n_{y,3} & n_{z,3} \\ n_{x,4} & n_{y,4} & n_{z,4} \\ n_{x,5} & n_{y,5} & n_{z,5} \end{pmatrix} \quad \text{and} \quad J = \begin{pmatrix} J_x \\ J_y \\ J_z \end{pmatrix}$$

where $n_{x,i}$, $n_{y,i}$, and $n_{z,i}$, i being between 1 and 5, are the Cartesian coordinates of the normal vector of the ith surface and J_x, J_y, and J_z are the Cartesian coordinates of the uniform field $\vec{J}$.

Data Availability Statement

The Swarm satellite data used in this study are available from ESA at http://swarm-diss.eo.esa.int/ http://swarm-diss.eo.esa.int/.

Acknowledgments
The authors wish to thank the two anonymous reviewers for their help in checking and improving the manuscript. This study was supported by the Centre National d'Etudes Spatiales (CNES) through the "Suivi et exploitation de la mission Swarm" project. M. Fillion is grateful to CNES for their support to his PhD grant. This work was supported in part by the NOAA Cooperative Agreement with CIRES, NA17OAR4320101.

References

Abidin, Z. Z., Jusoh, M., Abbas, M., Bolaji, O., & Yoshikawa, A. (2019). Features of the inter-hemispheric field-aligned current system over Malaysia ionosphere. *Journal of Atmospheric and Solar-Terrestrial Physics*, *192*, 104769. https://doi.org/10.1016/j.jastp.2018.01.012

Alken, P. (2016). Observations and modeling of the ionospheric gravity and diamagnetic current systems from CHAMP and Swarm measurements. *Journal of Geophysical Research: Space Physics*, *121*(1), 589–601. https://doi.org/10.1002/2015JA022163

Alken, P., Maus, S., Richmond, A. D., & Maute, A. (2011). The ionospheric gravity and diamagnetic current systems. *Journal of Geophysical Research*, *116*(A12), A12316. https://doi.org/10.1029/2011JA017126

Alken, P., Maute, A., & Richmond, A. (2017). The *F*-region gravity and pressure gradient current systems: A review. *Space Science Reviews*, *206*(1–4), 451–469. https://doi.org/10.1007/s11214-016-0266-z

Barlow, R. J. (1989). Statistics: A guide to the use of statistical methods in the physical sciences (Vol. 29, pp. 65–67). John Wiley & Sons.

Bolaji, O., Rabiu, A., Oyeyemi, E., & Yumoto, K. (2012). Climatology of the inter-hemispheric field-aligned currents system over the Nigeria ionosphere. *Journal of Atmospheric and Solar-Terrestrial Physics*, *89*, 144–153. https://doi.org/10.1016/j.jastp.2012.07.008

Chulliat, A., Vigneron, P., & Hulot, G. (2016). First results from the Swarm dedicated ionospheric field inversion chain. *Earth Planets and Space*, *68*(1), 104. https://doi.org/10.1186/s40623-016-0481-6

DeKeyser, J., Darrouzet, F., Dunlop, M. W., & Décréau, P. M. E. (2007). Least-squares gradient calculation from multi-point observations of scalar and vector fields: Methodology and applications with Cluster in the plasmasphere. *Annales Geophysicae*, *25*(4), 971–987. https://doi.org/10.5194/angeo-25-971-2007

Dunlop, M. W., Balogh, A., Glassmeier, K.-H., & Robert, P. (2002). Four-point Cluster application of magnetic field analysis tools: The Curlometer. *Journal of Geophysical Research*, *107*(A11), SMP 23-1–SMP 23-14. https://doi.org/10.1029/2001JA005088

Dunlop, M. W., Southwood, D., Glassmeier, K.-H., & Neubauer, F. (1988). Analysis of multipoint magnetometer data. *Advances in Space Research*, *8*(9), 273–277. https://doi.org/10.1016/0273-1177(88)90141-X

Dunlop, M. W., Yang, J.-Y., Yang, Y.-Y., Xiong, C., Lühr, H., Bogdanova, Y. V., et al. (2015a). Simultaneous field-aligned currents at Swarm and Cluster satellites. *Geophysical Research Letters*, *42*(10), 3683–3691. https://doi.org/10.1002/2015GL063738

Dunlop, M. W., Yang, Y.-Y., Yang, J.-Y., Lühr, H., Shen, C., Olsen, N., et al. (2015b). Multispacecraft current estimates at Swarm. *Journal of Geophysical Research: Space Physics*, *120*(10), 8307–8316. https://doi.org/10.1002/2015JA021707

Engels, U., & Olsen, N. (1998). Computation of magnetic fields within source regions of ionospheric and magnetospheric currents. *Journal of Atmospheric and Solar-Terrestrial Physics*, *60*(16), 1585–1592. https://doi.org/10.1016/S1364-6826(98)00094-7

Fathy, A., Ghamry, E., & Arora, K. (2019). Mid and low-latitudinal ionospheric field-aligned currents derived from the Swarm satellite constellation and their variations with local time, longitude, and season. *Advances in Space Research*, *64*(8), 1600–1614. https://doi.org/10.1016/j.asr.2019.07.022

Finlay, C. C., Maus, S., Beggan, C. D., Bondar, T. N., Chambodut, A., Chernova, T. A., et al. (2010). International geomagnetic reference field: The eleventh generation. *Geophysical Journal International*, *183*(3), 1216–1230. https://doi.org/10.1111/j.1365-246X.2010.04804.x

Finlay, C. C., Olsen, N., Kotsiaros, S., Gillet, N., & Tøffner-Clausen, L. (2016). Recent geomagnetic secular variation from Swarm and ground observatories as estimated in the CHAOS-6 geomagnetic field model. *Earth Planets and Space*, *68*(1), 112. https://doi.org/10.1186/s40623-016-0486-1

Friis-Christensen, E., Lühr, H., & Hulot, G. (2006). Swarm: A constellation to study the Earth's magnetic field. *Earth Planets and Space*, *58*(4), 351–358. https://doi.org/10.1186/BF03351933

Fukushima, N. (1979). Electric potential difference between conjugate points in middle latitudes caused by asymmetric dynamo in the ionosphere. *Journal of Geomagnetism and Geoelectricity*, *31*(3), 401–409. https://doi.org/10.5636/jgg.31.401

Fukushima, N. (1994). Some topics and historical episodes in geomagnetism and aeronomy. *Journal of Geophysical Research*, *99*(A10), 19113–19142. https://doi.org/10.1029/94JA00102

Harvey, C. C. (1998). Spatial gradients and the volumetric tensor. In P. Götz & W. D. Patrick (Eds.), *Analysis methods for multi-spacecraft data parameters* (pp. 307–322). ESA Publications Division.

Johnson, R. A. & Wichern, D. W. (2002). *Applied multivariate statistical analysis* (5th ed., pp. 663–667). Prentice Hall.

Kelley, M. C. (2009). Introductory and background material. In *The Earth's ionosphere: Plasma physics and electrodynamics* (chapter 1). Academic Press.

Lesur, V., Rother, M., Wardinski, I., Schachtschneider, R., Hamoudi, M., & Chambodut, A. (2015). Parent magnetic field models for the IGRF-12GFZ-candidates. *Earth Planets and Space*, *67*(1), 87. https://doi.org/10.1186/s40623-015-0239-6

Lühr, H., Kervalishvili, G., Michaelis, I., Rauberg, J., Ritter, P., Park, J., et al. (2015). The interhemispheric and F region dynamo currents revisited with the Swarm constellation. *Geophysical Research Letters*, *42*(9), 3069–3075. https://doi.org/10.1002/2015GL063662

Lühr, H., Kervalishvili, G., Rauberg, J., & Stolle, C. (2016). Zonal currents in the F region deduced from Swarm constellation measurements. *Journal of Geophysical Research: Space Physics*, *121*(1), 638–648. https://doi.org/10.1002/2015JA022051

Lühr, H., Kervalishvili, G. N., Stolle, C., Rauberg, J., & Michaelis, I. (2019). Average characteristics of low-latitude interhemispheric and F region dynamo currents deduced from the Swarm satellite constellation. *Journal of Geophysical Research: Space Physics*, *124*(12), 10631–10644. https://doi.org/10.1029/2019JA027419

Lühr, H., Rother, M., Maus, S., Mai, W., & Cooke, D. (2003). The diamagnetic effect of the equatorial Appleton anomaly: Its characteristics and impact on geomagnetic field modeling. *Geophysical Research Letters*, *30*(17), 1906. https://doi.org/10.1029/2003GL017407

Maeda, H. (1974). Field-aligned current induced by asymmetric dynamo action in the ionosphere. *Journal of Atmospheric and Terrestrial Physics*, *36*(8), 1395–1401. https://doi.org/10.1016/0021-9169(74)90216-5

Maus, S., & Lühr, H. (2006). A gravity-driven electric current in the Earth's ionosphere identified in CHAMP satellite magnetic measurements. *Geophysical Research Letters*, *33*(2), L02812. https://doi.org/10.1029/2005GL024436

Maus, S., Rother, M., Stolle, C., Mai, W., Choi, S., Lühr, H., et al. (2006). Third generation of the Potsdam Magnetic Model of the Earth (POMME). *Geochemistry, Geophysics, Geosystems*, *7*(7), Q07008. https://doi.org/10.1029/2006GC001269

Maus, S., Yin, F., Lühr, H., Manoj, C., Rother, M., Rauberg, J., et al. (2008). Resolution of direction of oceanic magnetic lineations by the sixth-generation lithospheric magnetic field model from CHAMP satellite magnetic measurements. *Geochemistry, Geophysics, Geosystems*, *9*(7), Q07021. https://doi.org/10.1029/2008GC001949

Maute, A., & Richmond, A. D. (2017a). Examining the magnetic signal due to gravity and plasma pressure gradient current with the TIE-GCM. *Journal of Geophysical Research: Space Physics*, *122*(12), 12486–12504. https://doi.org/10.1002/2017JA024841

Maute, A., & Richmond, A. D. (2017b). *F*-region dynamo simulations at low and mid-latitude. *Space Science Reviews*, *206*(1–4), 471–493. https://doi.org/10.1007/s11214-016-0262-3

Olsen, N. (1997). Ionospheric F region currents at middle and low latitudes estimated from Magsat data. *Journal of Geophysical Research*, *102*(A3), 4563–4576. https://doi.org/10.1029/96JA02949

Park, J., Luhr, H., & Min, K. (2011). Climatology of the inter-hemispheric field-aligned current system in the equatorial ionosphere as observed by CHAMP. *Annales Geophysicae*. *29*, 573–582. https://doi.org/10.5194/angeo-29-573-2011

Park, J., Yamazaki, Y., & Lühr, H. (2020). Latitude dependence of interhemispheric field-aligned currents (IHFACs) as observed by the Swarm constellation. *Journal of Geophysical Research: Space Physics*, *125*(2), e2019JA027694. https://doi.org/10.1029/2019JA027694

Press, W. H., Flannery, B. P., Teukolsky, S. A., & Vetterling, W. T. (1989a). *Numerical recipes* (2nd ed., pp. 656–661). Cambridge University Press.

Press, W. H., Flannery, B. P., Teukolsky, S. A., & Vetterling, W. T. (1989b). *Numerical recipes in C*. (2nd ed., pp. 61–70). Cambridge University Press.

Qian, L., Burns, A. G., Emery, B. A., Foster, B., Lu, G., Maute, A., et al. (2014). The NCAR TIE-GCM: A community model of the coupled thermosphere/ionosphere system. In *Modeling the ionosphere–thermosphere system* (pp. 73–83). American Geophysical Union (AGU). https://doi.org/10.1002/9781118704417.ch7

Richmond, A. D. (1995a). Ionospheric electrodynamics using magnetic apex coordinates. *Journal of Geomagnetism and Geoelectricity*, *47*(2), 191–212. https://doi.org/10.5636/jgg.47.191

Richmond, A. D. (1995b). The ionospheric wind dynamo: Effects of its coupling with different atmospheric regions. In *The upper mesosphere and lower thermosphere: A review of experiment and theory* (pp. 49–65). American Geophysical Union (AGU). https://doi.org/10.1029/GM087p0049

Rishbeth, H. (1971a). The F-layer dynamo. *Planetary and Space Science*, *19*(2), 263–267. https://doi.org/10.1016/0032-0633(71)90205-4

Rishbeth, H. (1971b). Polarization fields produced by winds in the equatorial F-region. *Planetary and Space Science*, *19*(3), 357–369. https://doi.org/10.1016/0032-0633(71)90098-5

Rishbeth, H. (1981). The F-region dynamo. *Journal of Atmospheric and Terrestrial Physics*, *43*(5), 387–392. (Equatorial Aeronomy - I). https://doi.org/10.1016/0021-9169(81)90102-1

Rishbeth, H. (1997). The ionospheric E-layer and F-layer dynamos—A tutorial review. *Journal of Atmospheric and Solar-Terrestrial Physics*, *59*(15), 1873–1880. https://doi.org/10.1016/S1364-6826(97)00005-9

Ritter, P., & Lühr, H. (2006). Curl-B technique applied to Swarm constellation for determining field-aligned currents. *Earth Planets and Space*, *58*(4), 463–476. https://doi.org/10.1186/BF03351942

Ritter, P., Lühr, H., & Rauberg, J. (2013). Determining field-aligned currents with the Swarm constellation mission. *Earth Planets and Space*, *65*(11), 9–1294. https://doi.org/10.5047/eps.2013.09.006

Sabaka, T. J., Tøffner-Clausen, L., Olsen, N., & Finlay, C. C. (2018). A comprehensive model of Earth's magnetic field determined from 4 years of Swarm satellite observations. *Earth Planets and Space*, *70*(1), 130. https://doi.org/10.1186/s40623-018-0896-3

Shen, C., Yang, Y. Y., Rong, Z. J., Li, X., Dunlop, M., Carr, C. M., et al. (2014). Direct calculation of the ring current distribution and magnetic structure seen by cluster during geomagnetic storms. *Journal of Geophysical Research: Space Physics*, *119*(4), 2458–2465. https://doi.org/10.1002/2013JA019460

Takeda, M. (1982). Three dimensional ionospheric currents and field aligned currents generated by asymmetrical dynamo action in the ionosphere. *Journal of Atmospheric and Terrestrial Physics*, *44*(2), 187–193. https://doi.org/10.1016/0021-9169(82)90122-2

Thébault, E., Finlay, C. C., Beggan, C. D., Alken, P., Aubert, J., Barrois, O., et al. (2015). International geomagnetic reference field: The 12th generation. *Earth Planets and Space*, *67*(1), 79. https://doi.org/10.1186/s40623-015-0228-9

Tøffner-Clausen, L., Lesur, V., Olsen, N., & Finlay, C. C. (2016). In-flight scalar calibration and characterization of the Swarm magnetometry package. *Earth Planets and Space*, *68*(1), 129. https://doi.org/10.1186/s40623-016-0501-6

vanSabben, D. (1970). Solstitial Sq-currents through the magnetosphere. *Journal of Atmospheric and Terrestrial Physics*, *32*(7), 1331–1336. https://doi.org/10.1016/0021-9169(70)90064-4

Vigneron, P., & Hulot, G. (2019). Towards correcting ASM data for the Sun-related thermoelectric effect. *Swarm 9th Data Quality Workshop Prague, Czech Republic*.

Vogt, J., Blagau, A., Bunescu, C., & He, M. (2020). Local least squares analysis of auroral currents. In M. W. Dunlop & H. Lühr (Eds.), *Ionospheric multi-spacecraft analysis tools: Approaches for deriving ionospheric parameters* (pp. 55–81). Springer International Publishing. https://doi.org/10.1007/978-3-030-26732-2_4

Vogt, J., Paschmann, G., & Chanteur, G. (2008). Reciprocal vectors. ISSI Scientific Reports Series (Vol. 8, pp. 33–46).

Vogt, J., Sorbalo, E., He, M., & Blagau, A. (2013). Gradient estimation using configurations of two or three spacecraft. *Annales Geophysicae*, *31*(11), 1913–1927. https://doi.org/10.5194/angeo-31-1913-2013

Yamashita, S., & Iyemori, T. (2002). Seasonal and local time dependences of the interhemispheric field-aligned currents deduced from the Ørsted satellite and the ground geomagnetic observations. *Journal of Geophysical Research*, *107*(A11), SIA 11-1–SIA 11-10. https://doi.org/10.1029/2002JA009414